7-29-2016

Characterizing the Transient Profile Shapes and Deposition Patterns of Desiccating Colloidal Droplets

Collin Taylor Burkhart
ctb6973@rit.edu

Characterizing the Transient Profile Shapes and Deposition Patterns of Desiccating Colloidal Droplets

By:

Collin Taylor Burkhart

A thesis submitted in partial fulfillment of
the requirements for the degree of Master of
Science in Mechanical Engineering

Department of Mechanical Engineering
Kate Gleason College of Engineering

Rochester Institute of Technology
Rochester, New York
Submitted July 29, 2016

Characterizing the Transient Profile Shapes and Deposition Patterns of Desiccating Colloidal Droplets

By:

Collin Taylor Burkhart

A thesis submitted in partial fulfillment of
the requirements for the degree of Master of
Science in Mechanical Engineering

Department of Mechanical Engineering
Kate Gleason College of Engineering

Approved by:

Dr. Michael Schertzer, Assistant Professor *Thesis Advisor, Department of Mechanical Engineering*	Date
Dr. Kara Maki, Assistant Professor *Committee Member, School of Mathematical Sciences*	Date
Dr. Michael Schrlau, Assistant Professor *Committee Member, Department of Mechanical Engineering*	Date
Dr. Agamemnon Crassidis, Graduate Director/Professor *Department Representative, Department of Mechanical Engineering*	Date

ABSTRACT

As a droplet containing colloidal material dries on a surface, the suspended particles are deposited onto it. Aqueous colloidal droplets often leave the majority of particles at the periphery of the deposition area. This phenomenon is known as the coffee ring effect, and it arises when a radially outward evaporative flows dominates within a droplet as it dries. This deposition non-uniformity can impact a diverse range of applications. In medical diagnostic testing, it can introduce uncertainty into microarray test results, while in inkjet printing it can produce finer printed circuitry. Controlling colloidal deposition could allow for higher-quality medical diagnostics and printing techniques.

Application of electric fields to evaporating droplets is a promising method for controlling the coffee ring effect. Applying a voltage across a droplet can produce electrowetting forces at the contact line and electrophoretic forces on suspended particles. These forces have the potential to influence contact line pinning, internal flows, and migration of particles within the droplet. Electric fields have previously been used to manipulate colloidal transport in droplets laden with a variety of particles. The present work experimentally characterizes the effects of the particle type, size, and actuation polarity on the contact line dynamics and resultant depositions of evaporating particle-laden droplets.

Deionized water droplets were seeded with a variety of particles and evaporated on an SU-8 photoresist substrates. Particle size was found to play a role in the final deposition patterns produced by carboxylate-modified polystyrene-laden droplets. Droplets with smaller particles repinned in the final stages of evaporation and produced ring depositions, while droplets with larger particles remained mobile and produced more uniform depositions. A comparison of the

evaporation times to particle settling times, showed that gravitational effects may influence the deposition behavior of larger particles. Particle material also plays a role in the resultant deposition pattern. Titanium oxide-laden droplets tended to pin longer and exhibited smaller receding contact angles as compared to polystyrene-laden droplets. Titanium oxide-laden droplets also tended to leave less distinct rings and large uniform regions in the final depositions. Actuation polarity was found to influence contact line mobility during the evaporation of particle-free and polystyrene-laden droplets. Polystyrene-laden droplets exposed to negative DC electric fields receded in a slip-stick pattern, while those exposed to positive DC electric fields receded more uniformly. No evidence of electrophoretic migration was observed, as both field polarities produced similar deposition patterns. Work is ongoing to quantify the electrophoretic effect.

ACKNOWLEDGEMENTS

I would first like to thank my advisor, Dr. Michael Schertzer. He first sparked my interest in this research nearly two years ago, and he has provided invaluable guidance and support throughout the entirety of thesis work since then. His door has always been open, and we have had a number of great discussions regarding things both inside and outside of the lab.

The members of my committee, Dr. Kara Maki and Dr. Michael Schrlau, have also taken an ongoing interest in my work, and the insights they have provided throughout this process are much appreciated. The weekly "lab talks" that Dr. Schrlau started these last several months have also been great opportunities to talk about my work and a good motivator to keep pushing forward.

I would also like to thank Peter Dunning, an alumnus of our lab. He helped to secure much of the equipment filling the Discrete Microfluidics Laboratory (DMFL) that I took for granted when I joined the lab. He also pioneered the device fabrication and imaging processes used here. Discussions with him about these processes and his experiments were very helpful when it fell to me to keep pushing the research forward and improving our processes after his graduation.

This work has been aided by a number of labs at RIT, but three in particular have been especially critical. The Semiconductor & Microsystems Fabrication Laboratory (SMFL) has played a fundamental role in creating the devices used. I would like thank Thomas Grimsley, Operations Manager of the SMFL, and the many technicians for their help in the development of our device fabrication process. The devices themselves were produced by the hard work of Hee Tae An and Rakesh Chokanathan. The fluorescent deposition imaging done in this work would not have been possible without the aid of Dr. Hyla Sweet and the Confocal Microscopy Laboratory (CML). I have been able to learn a lot from technicians Evan Darling, Lauren Heese, and Teresa

Zgoda, during long imaging sessions. The brightfield deposition imaging done in this work would not have been possible without the aid of Dr. Schrlau's Nano-Bio Interface Lab (NBIL). The NBIL has always generously offered to share equipment and resources, and I sincerely thank its many members who assisted me when I needed to image new depositions.

I would also like to extend my gratitude toward all of the professors in the Mechanical Engineering Department I have had for classes or worked with during my time at RIT. I am very happy to have the education and experiences they have given me. The department staff has also been extremely helpful, especially Jill Ehmann, William Finch, Hillary McCormick, and Diane Selleck.

While at RIT, I have also had the fantastic opportunity to meet a number of bright, motivated students, many of whom I now call my friends. Bryan, Dom, Eric, Hector, John, Nate, Nikki, Peter, Sam, Zinzer, and even Resnick, among so many others, have substantially shaped and added to my collegiate experiences over the last five years. It has also been especially nice to share research experiences with fellow graduate students, including Peter Dunning, Anna Jensen, Kaushik Kudtarkar, Olivia Scheibel, and many more. This research was not without difficulties, and it was always encouraging to know I was not alone.

Finally, I want to thank my family. My parents, grandparents, and other relatives have spent years helping me get to where I am today and have supported my pursuit of higher education. I am also especially grateful to Cammie Johanning, my fiancée and future member of the family, for providing unfailing support for all my endeavors over the past three-and-a-half years and helping me get to the end.

TABLE OF CONTENTS

LIST OF FIGURES

LIST OF TABLES

LIST OF APPENDICES

NOMENCLATURE

Bo	Bond number
c	Capacitance per unit area of the dielectric layer
D/D_0	Relative diameter
dF	Pinning force per unit length acting on the contact line
dF_a	Pinning force per unit length acting on the actuated contact line
g	Acceleration due to gravity
H	Initial height of the droplet
$I/\bar{I}$	Relative intensity
k	Proportionality constant
k_B	Boltzmann constant
k_D	Diffusion constant
m_p	Mass of a particle
R	Initial radius of the droplet
r/R	Relative radial position
R_p	Radius of the particle
Sr_z	Vertical Strouhal number
t	Evaporation time
T	Temperature
t_f	Total evaporation time
U_S	Stokes velocity in a stagnant flow
V	Magnitude of the applied voltage
v_i	Collapsing interface speed
v_p	Particle diffusion speed
x_p	Particle diffusion distance
γ_{lv}	Surface tension along the liquid-vapor interface
γ_{sl}	Surface tension along the substrate-liquid interface
γ_{sv}	Surface tension along the substrate-vapor interface
θ	Contact angle

θ_{eq}	Equilibrium contact angle
$\theta_{eq,a}$	Actuated equilibrium contact angle
θ_r	Receding contact angle
μ	Dynamic viscosity of the fluid
ρ	Density of the fluid
ρ_p	Density of the particle
τ_S	Stokes velocity time constant

1.0 INTRODUCTION

1.1 Background

Colloids are microscopic, insoluble particles evenly dispersed throughout another medium. Depending on the phases of the particles and medium, a colloid can be classified a number of ways, including as a foam like whipped cream, an emulsion like milk, or as an aerosol like fog and smoke. The field of colloidal science is dedicated to researching the intricacies of different colloidal systems. The present work focuses specifically on colloids consisting of solid particles dispersed in liquid media. As colloidal droplets evaporate, suspended particles deposit on the surfaces upon which they rest. The distribution of the deposited particles can impact a diverse range of applications, including medical diagnostics [1–7] and inkjet printing [8–10].

Deposition distribution can significantly impact the results of microarray testing. Microarrays are a type of lab-on-chip (LOAC) device. As a whole, LOAC devices seek to reduce as many laboratory functions as possible down to a single chip [11,12]. They reduce reagent cost by using smaller volumes of fluid [12,13] and tend to have shorter cycle times due to more favorable surface-area-to-volume ratios for mass transport [14]. Their portable, low-cost nature makes them well suited for overcoming two major issues preventing individuals from receiving necessary medical care: lack of access and affordability [15].

Microarrays consist of a chip covered with an array of droplets for high-throughput testing. Up to thousands of droplets can be deposited within a single square inch [16]. They revolutionized gene expression research by allowing an individual to sequence an entire genome on a single small slide [17]. Microarrays have also been used for detecting pathogens [1,2], determining antimicrobial resistances, and conducting enzyme-linked immunosorbent assays (ELISAs) [3].

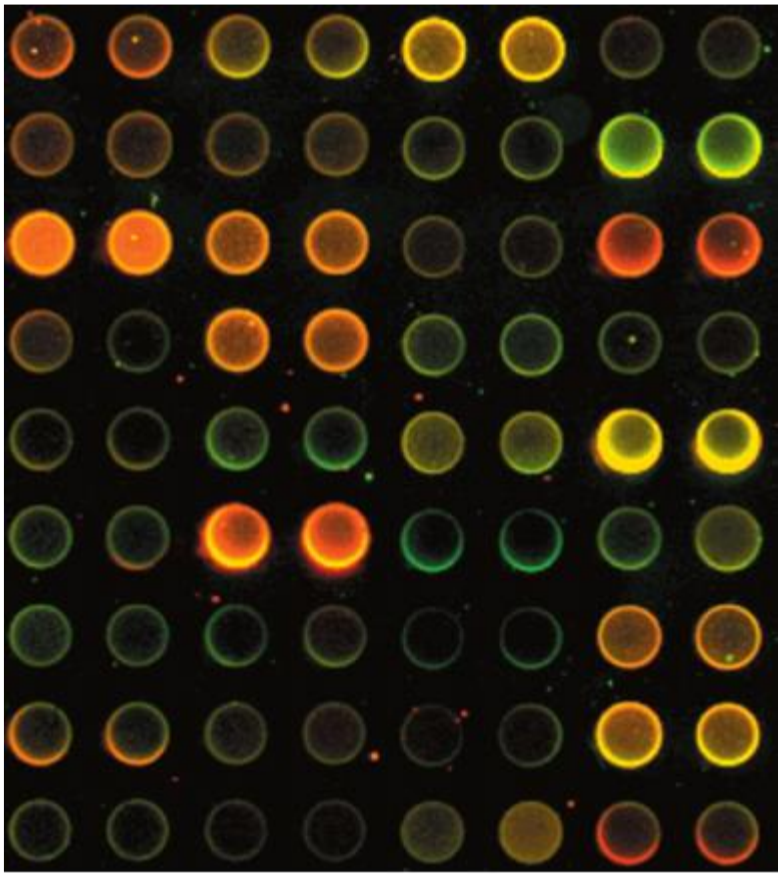

Figure 1.1 Fluorescent image of a cDNA microarray containing depositions from 72 droplets [7]. In each individual deposition, particles are concentrated at the outer periphery, as is evidenced by the bright outer rings.

Microarrays are commonly processed by measuring the fluorescence intensities of depositions deposited after evaporation [4,7]. The majority of the material often collects at the peripheries [4,7,18,19] (Fig. 1.1). This results in a non-uniform fluorescent intensity reading across the deposition which can negatively impact the accuracy and repeatability of analyses [4]. An improved understanding of the formation of microarray depositions and a potential means of control could improve the quality of microarray testing and may lead to improvements in testing accuracy and repeatability [1–7].

Colloidal transport and deposition is also important for advanced manufacturing of flexible

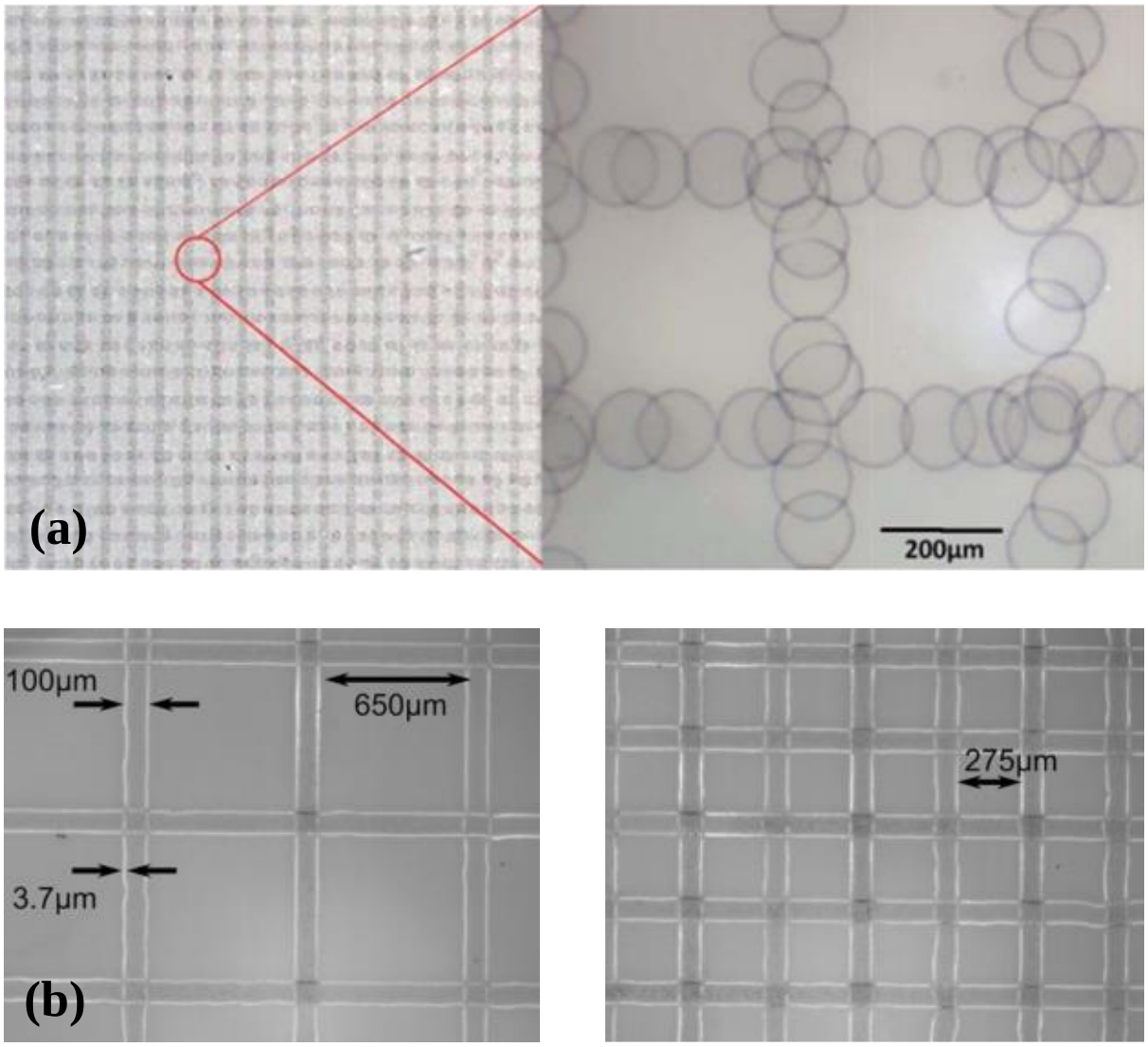

Figure 1.2 Conductive traces consisting of (a) overlapping rings [21] and (b) gridded parallel lines [8]. In both cases, the material is deposited primarily at the periphery of the printed areas due to the coffee stain effect. In (b) this phenomenon enables feature sizes up to two order of magnitude smaller than the printed line.

electronics. Such devices are commonly made by inkjet printing an ink containing conductive particles onto a flexible substrate [8,9]. The deposited conductive material forms the device circuitry. This circuitry has applications in flexible displays, bionic organs, and e-textiles [20]. As in microarrays, the conductive particles often deposit at the periphery of the depositions left by the printed ink. However, this can be leveraged to reduce printed feature sizes [8–10]. The

phenomenon can be used to produce arrays of overlapping rings from printed droplets (Fig 1.2a) to create flexible transparent conductive films for optoelectronic applications [9,21]. It can also be used produce "twin-line" depositions, pairs of parallel traces, from a single printed rivulet [8] (Fig 1.2b). Unfortunately, surface defects can produce non-uniformities at the periphery, and kinks in deposition lines are observable [8]. Here, a means of controlling the deposition pattern would be ideal in order improve print quality [8–10]. This could take the form of either suppressing the effect to coat the entire printed path uniformly or enhancing the effect to improve the deposition uniformity at the peripheries.

The deposition of the large majority of colloidal material at the periphery of the deposition area is known as the "coffee ring effect." The formation of coffee ring patterns was first characterized in the pioneering work of Deegan *et al*. [19,22,23], and is a result of complex interactions between a number of effects.

1.2 Literature Review

When a droplet rests on a surface, the shape it takes is determined by the relative strength of gravitational and capillary forces [24]. This relationship is quantified in the Bond number, *Bo*,

$$Bo = \frac{\rho_p g R H}{\gamma_{lv}}, \tag{1.1}$$

where ρ is the density of the fluid, g is the acceleration due to gravity, R is the initial radius of the droplet, H is the initial height of the droplet, and γ_{lv} is the surface tension along the liquid-vapor interface [25]. A small value indicates that surface tension forces dominate over gravitational forces, as is the case for droplets on the order of a millimeter in diameter. When this is the case, the droplet takes a spherical cap shape [8,25].

The outer ring where the droplet contacts the surface is known as the contact line (Fig. 1.3).

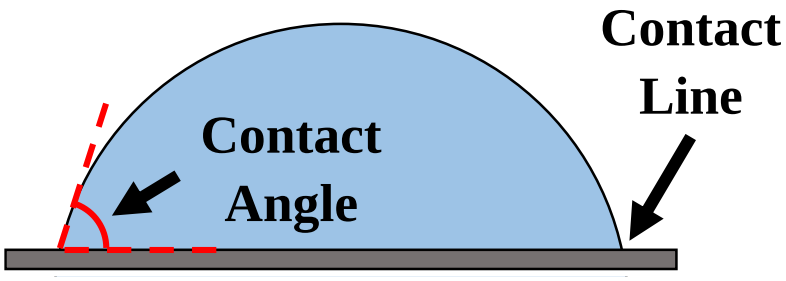

Figure 1.3 The contact line and contact angle of a droplet resting on a surface. The contact angle is measured through the droplet.

The angle that the droplet makes with the surface, measured through the droplet, is the contact angle. If the surface is hydrophilic, the contact angle is small and the droplet is flatter. If it is hydrophobic, the contact angle is large, and the droplet sits higher on the surface [24]. When a droplet is at equilibrium, it exhibits its equilibrium contact angle, θ_{eq}. This is also known as the Young's angle and can be calculated using the Young equation [26,27],

$$\gamma_{sv} = \gamma_{sl} + \gamma_{lv} \cos \theta_{eq}, \tag{1.2}$$

which equates the surface tension forces at the contact line in a droplet-substrate system (Fig. 1.4). Here, γ_{sv} and γ_{sl} are the surface tensions along the substrate-vapor and substrate-liquid interfaces, respectively.

On a perfect surface, the shape of an droplet would always be characterized by the equilibrium contact angle, and its height and diameter would change as its volume increased or decreased [28]. On real surfaces, droplet contact lines become pinned in place due to random surface defects [23,29]. As such, changes in droplet volume can result in changes in the apparent contact angle. The upper and lower limits the angle can assume are known as the receding and advancing contact angles, respectively, and the difference between the two is the contact angle hysteresis [28,30]. Further volume change after reaching either limit results in contact line motion. The contact line slips as the surface tension forces overcome the pinning forces, and the droplet

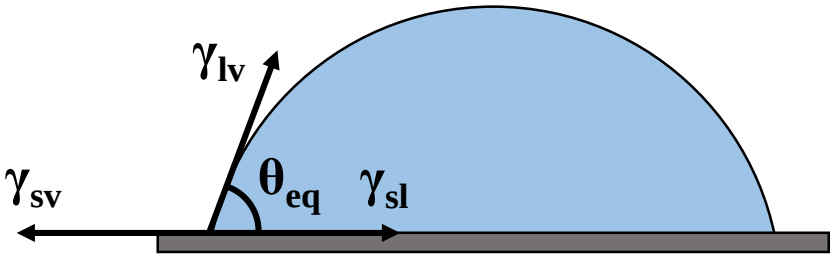

Figure 1.4 The surface tension forces acting in a droplet-substrate system. When no outside forces act on the droplet, it takes the equilibrium, or Young's, contact angle.

begins to advance or recede [31]. Depending on the rate of volume change and how much the pinning forces can increase in response, the droplet can stick and slip a number of times [23].

One common cause of volume change is evaporation. Here, aqueous droplets lose volume over time. As this occurs, three general evaporation regimes can be exhibited [28,32] (Fig. 1.5). In the constant contact diameter (CCD) regime (Fig. 1.5a), the droplet remains pinned and the contact angle reduces. Due to the presence of pinning forces, aqueous droplets often initially evaporate in this regime until reaching their receding contact angles. In the constant contact angle (CCA) regime (Fig. 1.5b), the contact line recedes as the angle holds stable. Aqueous droplets can exhibit this mode after a CCD regime once they reach their receding contact angles. In the mixed regime (Fig. 1.5c), both contact angle and diameter decrease. In aqueous droplets, the CCA regime can lead into a mixed regime if the contact angle begins decaying along with diameter, or it can reenter a CCD regime if the droplet repins.

Evaporation plays a significant role in the coffee ring effect phenomenon. Pinned aqueous droplets in air generally undergo evaporation limited by diffusion of vapor away from the interface [18,23]. As such, the evaporation rate over the droplet surface is highest along the contact line. If the contact line is pinned, the evaporation gradient drives a radially outward flow within the droplet to compensate for mass lost at the periphery (Fig. 1.6). Even when evaporation is uniform over the droplet surface, a radially outward flow is still required to conserve mass at a pinned contact

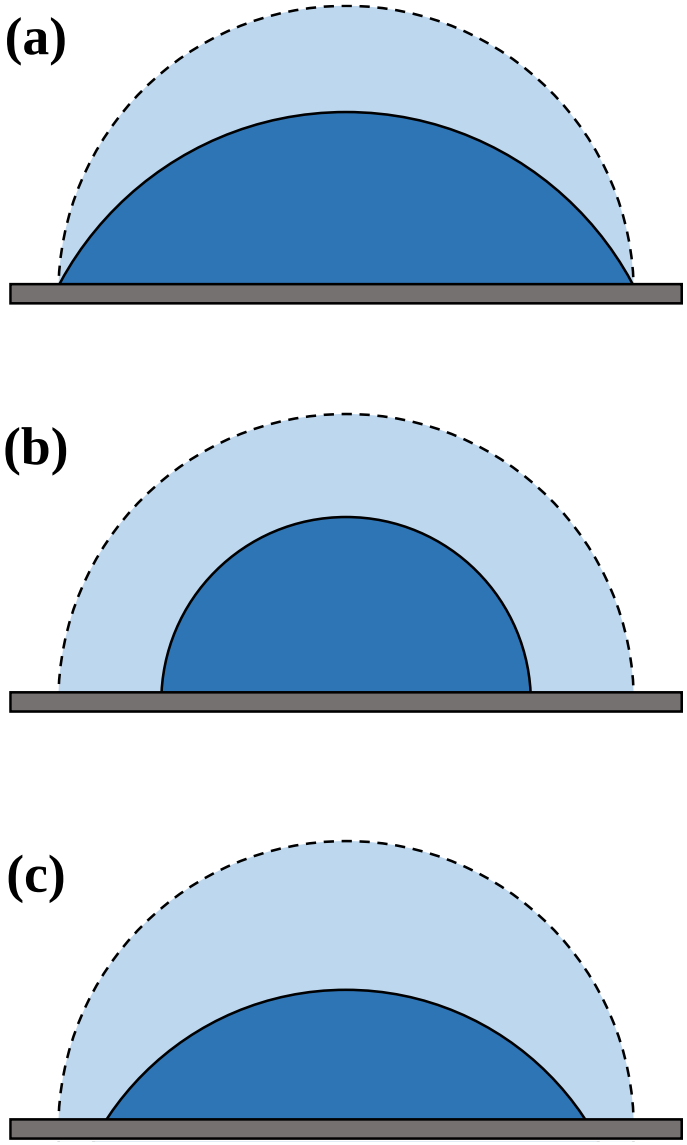

Figure 1.5 Droplets evaporating on substrates do so in three general regimes: (a) the constant contact diameter (CCD) regime, (b) the constant contact angle (CCA) regime, and (c) the mixed regime. The lighter-blue regions bounded by dotted lines show the initial droplet positions. The darker-blue regions bounded by solid lines show the positions after the droplets have evaporated for some time.

line since the droplet interface collapses less than near the center of the droplet. In either case, the radially outward flow can carry any suspended particles to the contact line where they deposit. This results in coffee ring formation. Particle buildup at the periphery can also augment the pinning forces and extend the length of the CCD regime [31].

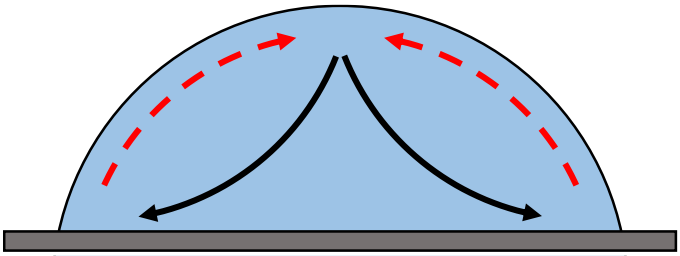

Figure 1.6 The competition between the evaporative and Marangoni flows within a pinned evaporating droplet. Evaporative flows are shown in solid black, and Marangoni flows are shown in dashed red. Marangoni flows are shown to inhibit the evaporative flow, but they can enhance it under particular droplet and ambient conditions.

While evaporation can drive a peripheral flow, it also can create a temperature gradient over the droplet profile which can produce a surface tension-driven Marangoni flow [33,34] (Fig. 1.6). Temperature differences between the substrate and the ambient air can also contribute the temperature gradient driving this flow. The Marangoni flow can enhance or impede the evaporation-driven flow [35]. When it counters the evaporative flow, it can resuspend particles rather than allow them to be carried to the contact line. When strong enough, Marangoni forces can even produce a "skin of particles" at the outer layer of the droplet. When these transport mechanisms compete and the evaporative flow dominates, coffee ring patterns are produced.

In addition to the two effects shown in Figure 1.6, Derjaguin-Landau-Verwey-Overbeek (DLVO) interactions can also influence the deposition patterns formed. These interactions describe the van der Waals and electrostatic forces acting in the droplet system [36]. The surface charges of suspended particles and the substrate can cause particle-particle repulsion and particle-substrate repulsion or attraction when objects are separated by distances on the order of the Debye length. The surface charge also influences the thickness of the electric double layer formed around each particle. This varies the range at which these attractive and repulsive forces act.

It has been suggested that the ultimate deposition pattern left by evaporating colloidal droplets is governed by the relative strengths of the evaporative flow, the Marangoni flow, and the

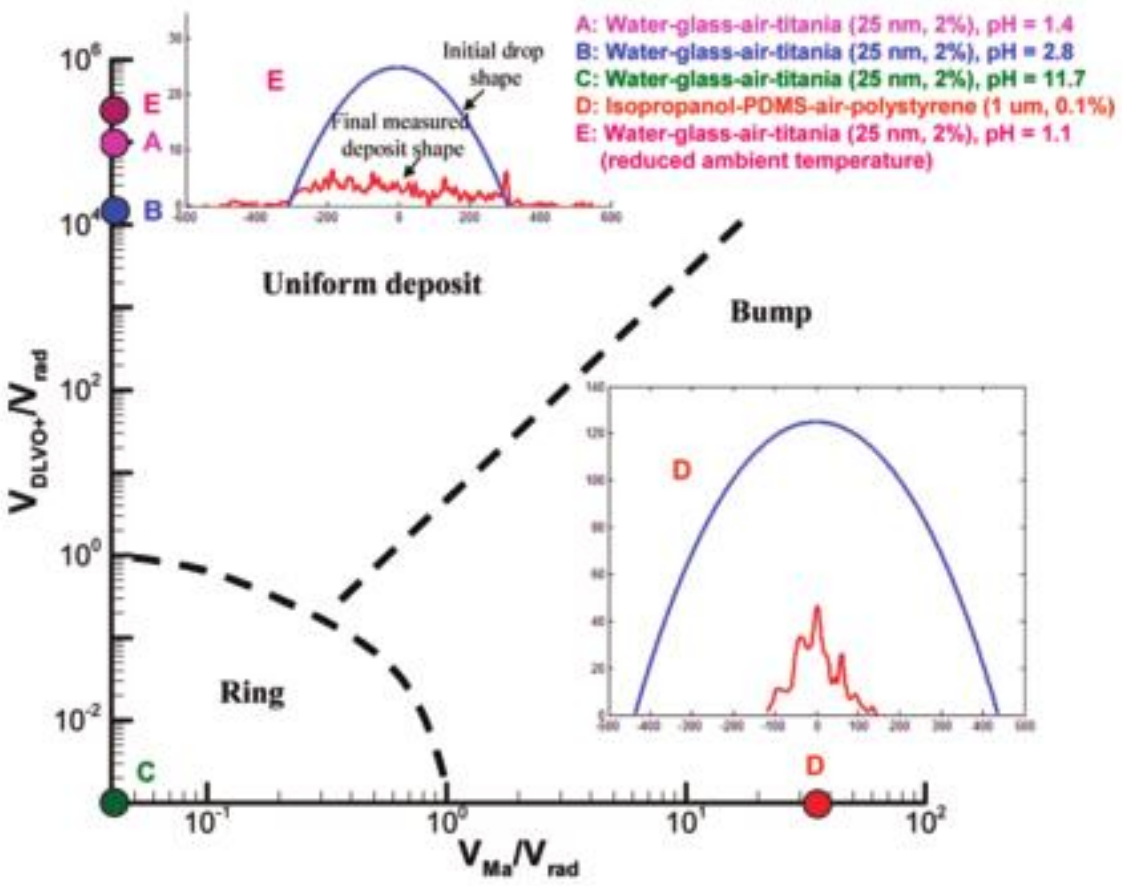

Figure 1.7 A proposed flow map showing the deposition formations produced in different dominant flow regimes [36]. Ring depositions are produced when evaporative flows dominate (V_{rad}), bump depositions form when Marangoni flows dominate (V_{Ma}), and uniform depositions form when DLVO forces dominate (V_{DLVO+}).

DLVO forces (Fig. 1.7). The coffee ring pattern is observed when the evaporative flow is dominant. When Marangoni effects dominate, a smaller central bump pattern is deposited at the center of the original droplet. A uniform deposition pattern is observed when attractive DLVO forces dominate.

It would be advantageous to control the coffee ring effect in evaporating droplets for many applications, including medical diagnostic testing [1–7] and inkjet printing [8–10]. Many investigations have previously sought to suppress the coffee ring effect to improve deposition uniformity [37–39]. Surfactants [40] and temperature gradients [41,42] have been used to

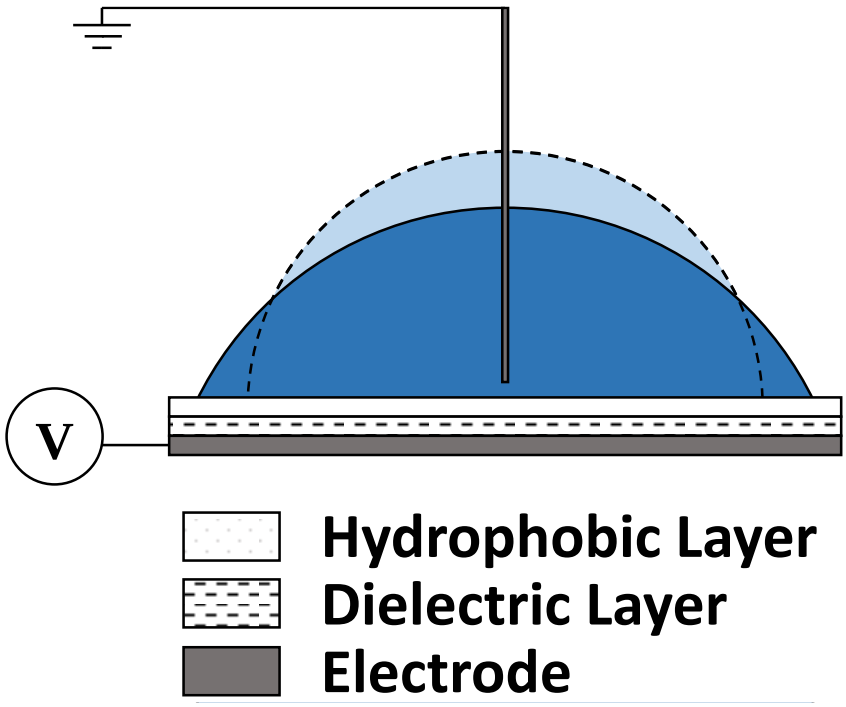

Figure 1.8 A typical setup for using electric fields to control colloidal deposition in an evaporating droplet. The lighter-blue region bounded by a dotted line shows the initial droplet position before actuation. The darker-blue region bounded by a solid line shows the actuated position caused by electrowetting. An AC signal can be used in place of the DC one shown.

influence to the internal Marangoni flow to counter the evaporative flow. Particle shape modification [43] has been utilized to inhibit contact line pinning. DLVO forces have been manipulated to control deposition formation by adjusting pH to change particle surface charge [36].

This work focuses on the application of electric fields as a means of evaporation and deposition formation control. This method can utilize both AC [37,38] and DC [44] fields. A typical setup for the application of an electric field on an evaporating droplet is shown in Figure 1.8. A particle-laden droplet is deposited onto a coated electrode. The electrode is coated with a dielectric layer and then with a hydrophobic layer, though a single composite material can serve as both. A ground wire is inserted into the top of the droplet. A voltage is applied to the electrode as the droplet is allowed to evaporate.

In both AC and DC configurations, droplets experience electrowetting effects. When the voltage is applied, a force is applied at the contact line which deforms the droplet interface and results in a higher degree of wetting on the surface [24]. The droplet increases in diameter and decreases in both height and apparent contact angle. The dielectric layer serves to delay the onset of electrolysis in the droplet during actuation [38]. The hydrophobic layer causes droplets to have larger equilibrium contact angles which allows for a more change during actuation [45].

An electrowetting induced change in the interface shape can influence the evaporation of the droplet, as evaporation depends upon droplet geometry [22,23]. The change in apparent contact angle is described by the Berge-Lippmann-Young (BLY) or electrowetting equation [24],

$$cos\theta_{eq,a} = cos\theta_{eq} + \frac{cV^2}{2\gamma_{lv}}, \tag{1.3}$$

where $\theta_{eq,a}$ is the actuated equilibrium contact angle, c is the capacitance per unit area of the dielectric layer, and V is the magnitude of the applied voltage. This is also known as the modified Young equation, as it can be derived from the Young Equation (Eq. 1.2) by adding an additional electrowetting force at the contact line. The voltage term in the BLY equations is also known as the electrowetting number [37,38]. While this relationship accurately predicts smaller apparent contact angle changes, it is known to break down once the apparent contact angle reaches a system-dependent saturation point where further increases in voltage produce little or no change [46,47].

When AC fields are applied to an evaporating droplet, the electrowetting force on the contact line is not constant. Instead, it changes with the frequency of the field. This oscillatory force can delay the onset of contact line pinning at lower frequencies on the order of 10 *Hz* [37–39]. This allows droplets to recede longer before repinning and can produce smaller depositions. As actuation frequency increases, on the order of 1 *kHz*, the oscillation can also begin to generate electrothermal flows as the electric field penetrates into the droplet and creates temperature

gradients. These flows can counteract the evaporative flow driving the coffee ring effect. However, as frequency increases even further, on the order of 100 *kHz*, inertial limits result in less net motion of the droplet. Here, no advantage is gained by employing an alternating signal.

When DC fields are applied, additional forces can be applied on any suspended particles in the droplet to produce more uniform deposition patterns [44]. When the polarity of the actuated electrode is opposite the charge of the suspended particles, the particles experience an attractive electrophoretic force. This can carry particles downward toward the substrate before they can be swept to the periphery by the evaporative flow. This has also been observed to result in increased contact line mobility. The decrease in particle accumulation at the contact line results in fewer slip-stick cycles during evaporation.

Electric fields have two key advantages over other means of control. First, no permanent modification to the droplet is necessary. The applied fields can easily be deactivated by turning off the applied voltage, and the droplet at no point changes composition. Second, electrical fields act are fast acting. The electrowetting effect occurs in a fraction of a second once the field is applied.

1.3 List of Contributions

The goal of this investigation is to characterize further the impact of particle selection on colloidal transport in evaporating droplets. Experiments primarily focus on the roles of particle size and type in colloidal deposition on hydrophobic surfaces. The influence of voltage polarity in evaporation with an applied DC electric field is also investigated. Particle types and sizes selected are typical of those currently used in medical diagnostic and printing applications where deposition control is critical. To these ends, this work makes four primary contributions.

1. A method for repeatably quantifying the deposition distribution patterns left after droplet

evaporation (Sec. 3.4)

2. A study of the effect of particle size and type where gravitational effects were quantified and found to play a non-negligible role in the colloidal transport of large particles (Secs. 4.1 and 4.2)
3. Preliminary results investigating the role of DC actuation polarity where transient profile behavior was found to depend on the polarity in both pure liquid and particle-laden droplets (Sec. 4.3)
4. A variety of publications sharing the methodology and results presented in this work, including four conference proceeding publications and an in-progress journal paper (App. A.1)

2.0 RESEARCH QUESTION

The primary goal of this thesis is to answer the following question: **What are the effects of particle selection on colloidal transport in evaporating droplets?** This work seeks to answer this by experimentally characterizing the effects of particle size, density, and concentration on transient droplet evaporation and final deposition distribution. Particles used are selected due to their common use in applications where particle deposition is critical. This work also presents preliminary data on the impact of DC voltage polarity on electrically actuated evaporation.

An improved understanding of how a suspended particle impacts the contact line dynamics and internal flows of its droplet medium, as well as how it can interact within an electric field applied to the droplet, is vital for developing more sophisticated means of colloidal transport control. Improved control could enhance deposition quality in existing colloidal transport applications as well as enable the development of novel techniques for nanoparticle assembly. Electric fields have previously been used to manipulate colloidal transport and influence coffee-ring formation in droplets laden with particles of several types and ranging in size and concentration [37,38,44]. However, the isolated impact of particle selection on unactuated droplet desiccation has not been studied in as great detail. Further, no distinction is made between the impact of a positive and a negative actuating polarity in DC-actuated electrowetting.

3.0 EXPERIMENTAL METHODOLOGY

This chapter details the five components of the experimental facility used in this investigation. The methods for creating the droplets and devices are outlined, the equipment for data collection are listed, and the analyses performed on the transient data and final deposition patterns are explained. A diagram of the general experimental setup employed is presented in Figure 3.1.

3.1 Droplets

The solvent used in all droplets in these experiments is deionized (DI) water. DI water is primarily processed in the Semiconductor & Microsystems Fabrication Laboratory (SMFL) at the Rochester Institute of Technology (RIT). Conductivity of the water is regularly monitored to be between 17.9 $M\Omega \cdot cm$ and 18.2 $M\Omega \cdot cm$. Later experiments using higher concentrations of particles were made using type II DI water from ChemWorld.

In some cases, the DI water is seeded with particles to form the droplet solution. Particles are either yellow-green fluorescent, carboxylate-modified polystyrene microspheres from Life Technologies or titanium oxide nanopowder from Sigma Aldrich. Polystyrene particles are one of three sizes in diameter: 25 *nm*, 63 *nm*, or 1.1 μm. Titanium oxide particles are 21 *nm* in diameter. A 2% aqueous stock solution of polystyrene particles is diluted using DI water to achieve the desired volume fraction. The stock solution is sonicated in a Bransonic 1800 ultrasonic bath for 15 minutes prior to dilution. Titanium oxide solutions are created by weighing a mass of titanium oxide nanopowder and adding it to DI water. Experiments comparing particle sizes utilize 0.05% polystyrene-laden droplets. Experiments comparing polystyrene and titanium oxide droplets have

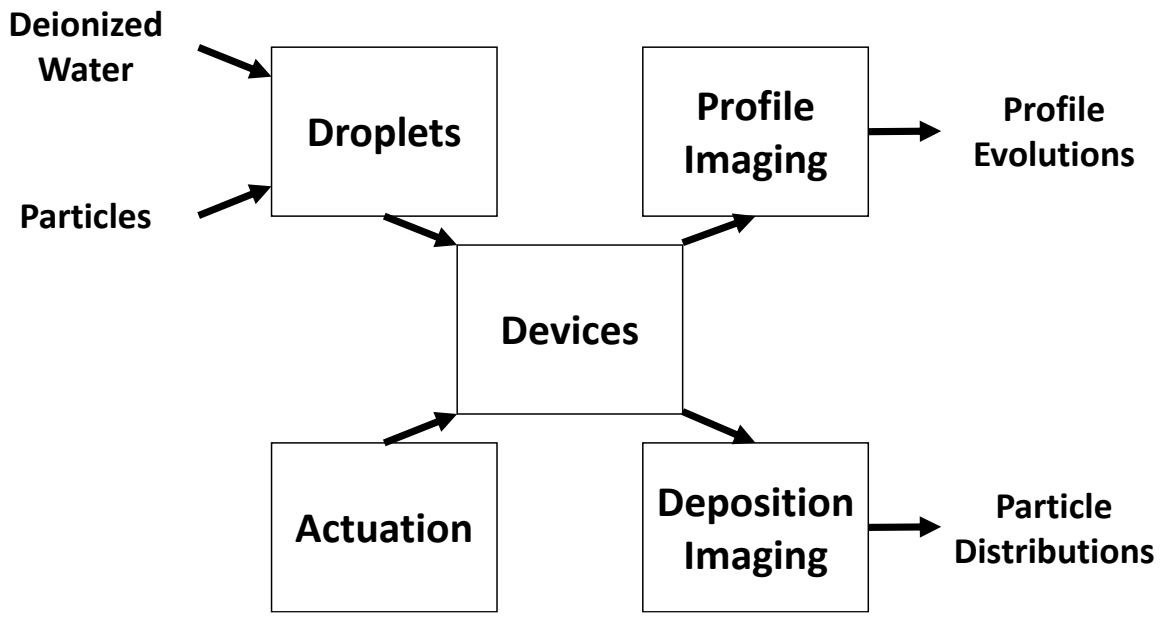

Figure 3.1 Experimental setup diagram.

a volume fraction of 0.02%. Higher-concentration solutions of titanium oxide were observed to have particles fall out of solution in tens of seconds. Experiments comparing the effects of actuation polarity at different particle concentrations utilize a range of polystyrene concentrations from 0.02% to 0.2%. All solutions are sonicated for 15 minutes prior to experimental use to improve solution uniformity. In all cases, 1 μL droplets are drawn and deposited onto the evaporation substrate using an Eppendorf Research Plus micropipette. Uncertainty in deposited volume is reported at ±3% by the micropipette manufacturer.

3.2 Devices

The two device designs used in this investigation are diagrammed in Figure 3.2. All devices are fabricated in the SMFL. A more detailed procedure for the processing steps outlined here is found in Appendix B. Devices for unactuated trials consist of two layers (Fig. 3.2a,c). The base of each device is a commercially purchased Corning plain glass microscope slide, 75 *mm* x 50 *mm* in size. Slides are cleaned by rinsing them with three solutions consecutively to remove

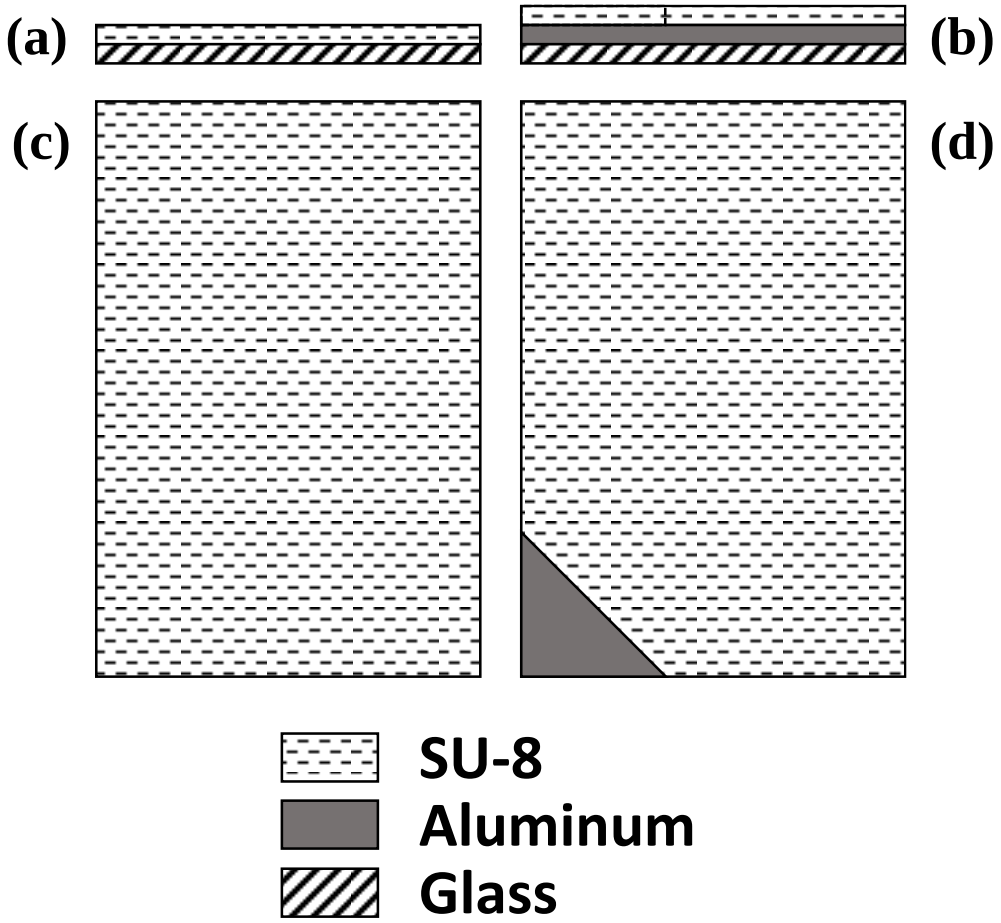

Figure 3.2 Device (a,b) side-view diagrams and (c,d) top-view diagrams of the two device designs used. The exposed electrode required for actuation incorporated into the 3-layer device design can be observed in (d).

oils and organic contaminants: first with acetone, then with isopropyl alcohol, and finally with DI water. Cleaned devices are then dried by nitrogen spray gun. A 3.0 to 4.0 μm layer of SU-8 3005 negative photoresist from MicroChem is then spun onto the slides using an SCS model 6700 manual photoresist spin coater. Coated slides are soft baked to promote adhesion. Devices are then exposed to reduce solubility in the SU-8 and subjected to a post-exposure bake to further improve adhesion. Finally, devices are developed using SU-8 developer and then hard baked to finish the device for use. Droplets deposited onto the finished SU-8 coating were observed to

exhibit initial contact angles of approximately 89°.

For actuated trials, devices need an additional metal layer between the glass and photoresist (Fig. 3.2b,d). Once the glass slides are cleaned, a layer of aluminum approximately 1 μm thick is deposited onto them using a CVC 601 sputter system. This forms the electrode. The metal-coated devices are then subjected to the remainder of the processing as before with one exception. During exposure, one corner of the device is covered with aluminum foil to mask it. This covered area is never exposed to UV light so the solubility of the SU-8 beneath is not reduced. During development, the SU-8 in this area dissolves and leaves exposed aluminum. This allows for later electrical access to the electrode. The thickness of the remaining SU-8 is measured using a Tencor P2 profilometer. Since the SU-8 serves as the dielectric layer, variation in the thickness results in changes in the droplet deformation exhibited when actuated as described by the Berge-Lippmann-Young (BLY) equation [47,48] (Eq. 1.3).

3.3 Profile Imaging

Droplets profiles are imaged as shown in Figure 3.3. Devices are positioned on the stage of a Ramé-Hart model 250 goniometry system once droplets are deposited onto them. The goniometry system consists of a backlit 5-axis stage (x-y-z-pitch-roll) and a CCD camera (659x494 pixels) (Fig. 3.3a). The system is leveled and the stage locked into place prior to each set of experiments. The stage is then brought into focus so the droplet edge is crisp. Side-view images of the droplet interface recorded (Fig. 3.3b) at one frame per second.

Images from the Ramé-Hart system are analyzed using Ramé-Hart DROPimage Advanced software. The program detects the droplet in the captured image and optically calculates the droplet's width and contact angle for that frame (Fig. 3.3b). The measurement scaling of the system is verified prior to experimentation. The contact angle provided is the average of the

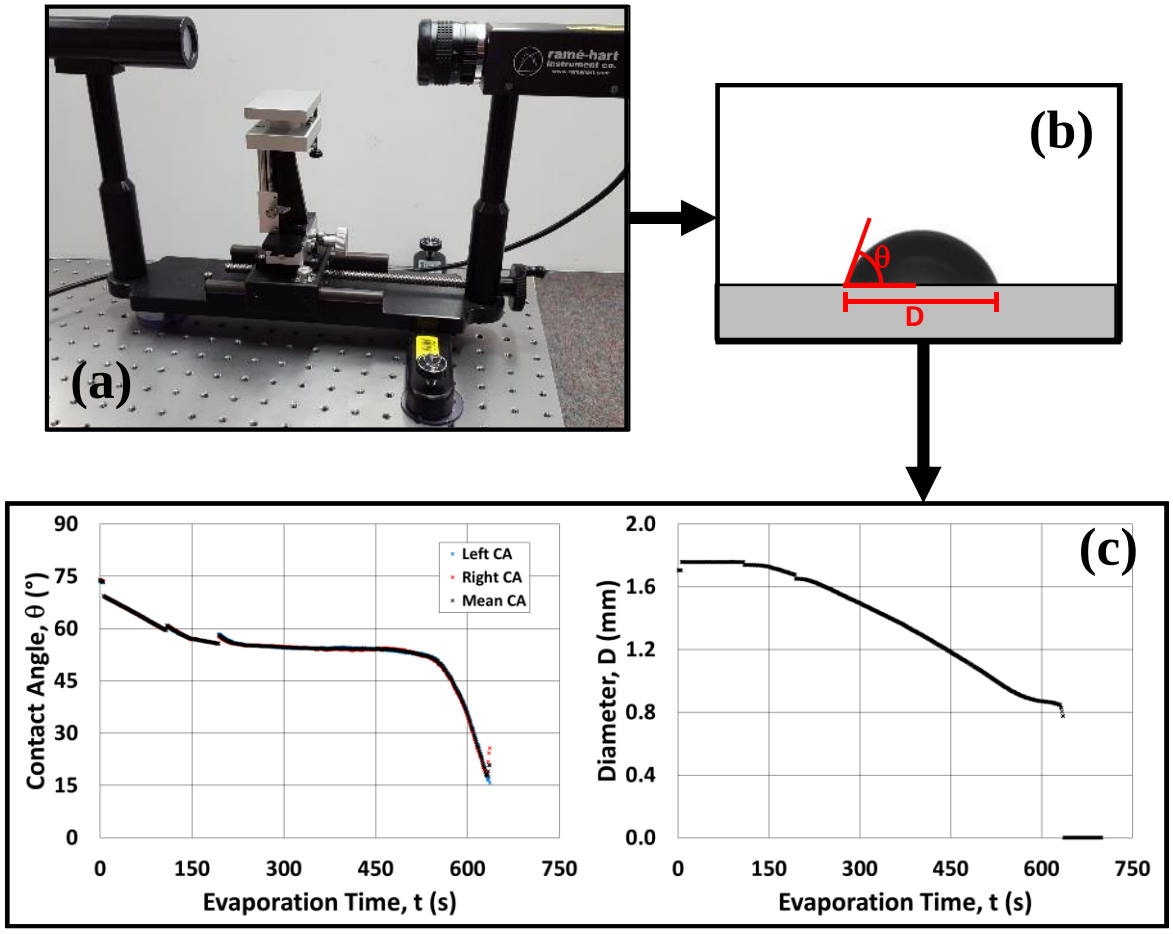

Figure 3.3 The profile imaging procedure consists of (a) a backlit stage where droplets are evaporated and a camera capturing side-view images of the droplet. Contact angles and diameters are calculated from (b) each captured frame of the droplet profile. Values from all frames over the course of evaporation can be combined to show (c) plots of profile evolution for each droplet.

contact angles on the left and right sides of the droplet. The diameter is taken to be the widest portion of the identified droplet area. The area is identified based on a manually entered droplet centerline and a high contrast between the white background and dark droplet (Fig. 3.4). The brighter the backlight, the starker the contrast and the easier it is for the software to detect the droplet area. However, a bright light also produces a white spot at the droplet center that can interfere with measurements. Lighting is adjusted manually between trials to keep the lighting as low as possible while still maintaining a clear contrast between the droplet and background. The

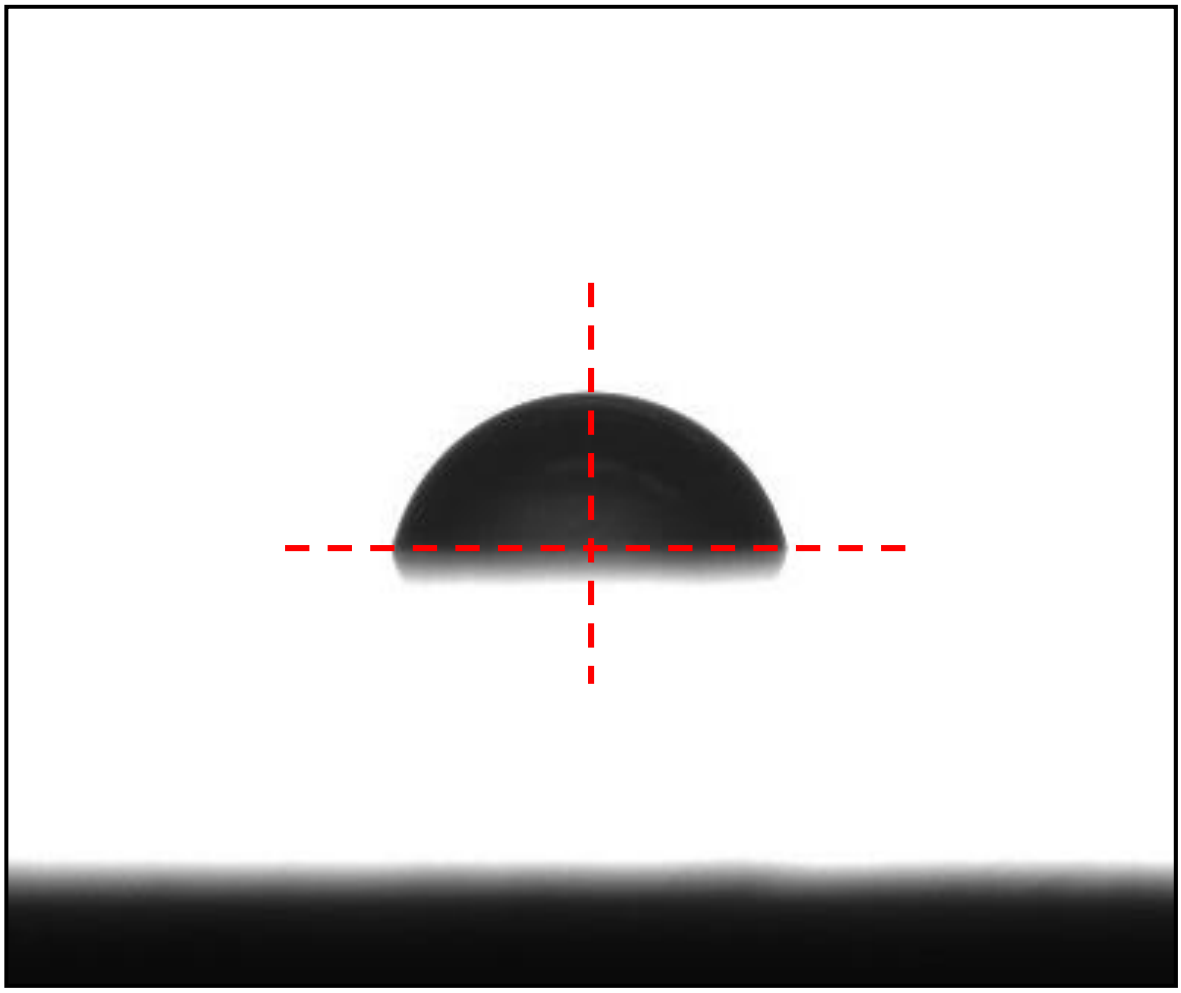

Figure 3.4 A frame captured during profile imaging. The vertical and horizontal dotted red lines show sample locations of the centerline and baseline, respectively, that a user must enter when running the Ramé-Hart software to calculate contact angles and diameters correctly. The dark area immediately below the baseline is a reflection of the droplet on the device surface.

camera also picks up a reflection of the droplet on the device, so a baseline must also be manually entered for the program to discard the duplicate portion (Fig. 3.4). Over the course of droplet evaporation, the program creates a log file of the changing contact angles and diameters as images are taken which can be used to plot transient profile behavior (Fig. 3.3c). This entire profile imaging process is repeated for at least five trials of each case.

Several issues can arise during profile imaging. In any given trial, the droplet can shift toward one side on the device as it evaporates due to asymmetric pinning. If the droplet shifts left

or right, the manually entered centerline can eventually leave the droplet area, so the software can no longer take measurements. Additionally, for droplets with initial contact angles close to 90° as are used here, it can be difficult to identify the baseline at the start of a trial. Choosing a baseline too high cuts off part of the droplet, while choosing one too low includes part of the droplet reflection on the substrate. It is not feasible to adjust the horizontal and vertical positioning of the stage manually during testing. However, the Ramé-Hart software allows for recalculation of contact angles and diameters from the saved images of a previous trial. The manually entered droplet centerline and baseline can be adjusted each time to resolve any mispositioning, should it occur.

Another issue arises near the end of each trial when the droplet becomes very small. The DROPimage Advanced software can have difficulties accurately measuring flatter droplets with contact angles below 20°[33]. Errors in size measurements at the smaller scale propagates when fitting a tangent line to the droplet profile. Further, at small sizes the program can misperceive where the droplet is located and instead detect stray debris or an out of plane deposition in place of the actual droplet. The program then outputs false measurements of the debris or deposition instead of the droplet as desired. The detected droplet area and contact angles are shown in the software during operation, so it can readily be observed by a user when this error occurs. In the log files, these errors can often be identified as an unusually large contact angle or diameter, sometimes much larger than the initial values. Recalculating and slightly adjusting the centerlines and baselines can minimize the number of stray readings or eliminate them entirely.

A final issue with this process is that the droplet can also shift forward or backward on the device as it dries. This results in the droplet shifting slightly out of focus and the formerly crisp edges in the recorded images becoming blurred. This makes it more difficult for the software to

detect the true droplet interface and can introduce error into the measurements taken. It is not feasible to adjust the focus manually throughout the course of evaporation. Currently it is accepted that this introduces a degree of error into the profile measurements when reviewing the results. This is part of the reason that multiple trials are always performed, as they can be used to quantify profile data repeatability.

After each set of trials, the stored images are reviewed and recalculated to minimize the effects of droplet shifting and detection that may have arisen during the trials. The final frame in which the droplet is visible is also recorded for each trial. The new log files and evaporation times are then imported into an Excel spreadsheet for data analysis. Any portions of data in the log files where the software recorded an error are deleted. These entries can be denoted as having errors in the profile data, errors in calculation, or errors in detecting the droplet edge.

A pair of master plots for the set of trials showing the progression of contact angle and diameter generate automatically. Because each experiment can take a different amount of time to start due to differences in focusing and positioning times, the trials are aligned based upon the end of evaporation. This time can be ascertained directly from the recorded images. The end-aligned data sets are then averaged. The mean values and three standard deviations above and below are plotted to show the general trend and spread for the entire set. Diameter and time values are normalized relative to the initial diameter and total evaporation time of the longest trial. The normalized plots allow for quantitative comparison of data from different experimental cases.

Dimensional plots are also generated for each individual trial. These are reviewed to ensure no one particular trial is substantially altering the mean plots. If one trial's plots appear significantly different from the rest, the evaporation images for that trial are reviewed and recalculated to ensure they were processed correctly. This also allows for the identification of an

error in the trial for which it should be discounted. If, for instance, it is found that the DROPimage software repeatedly measures debris instead of the droplet and cannot be corrected by adjusting the centerline and baseline, the trial is discounted.

3.4 Deposition Imaging

Deposition imaging is performed using two different microscopes. Both systems are operated on vibration isolation tables to minimize vibrational effects during imaging. Detector gain for each system is adjusted between cases to minimize noise without oversaturating the recorded images.

Fluorescent images of depositions left by polystyrene-laden droplets are taken using a Leica SP5 spectral confocal laser scanning microscope located in the Confocal Microscopy Laboratory (CML) at RIT. Depositions are first excited at the manufacturer-recommended wavelength using an argon laser with an acousto optical tunable filter. A Leica HyD detector then images the excited depositions. Captured images have a bit depth of 12 and have resolutions of at least 2048x2048 pixels. The images have black backgrounds and yellow-green depositions. Image intensity is used as a proxy for particle concentration, as more particles fluoresce more intensely than fewer particles.

Depending on the particles used, the captured image can vary substantially with the height of the imaging plane (Fig. 3.5). This is due to the fact that the depositions are not flat or nearly flat. To accommodate for this variation, ten images at different heights are captured for each deposition. A single maximum projection of the ten images is then used as a representation of the

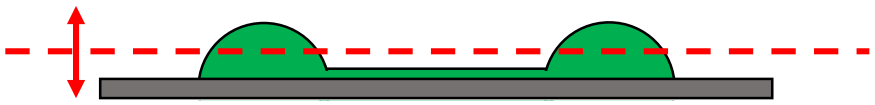

Figure 3.5 Polystyrene-laden droplets can leave depositions that vary with height, shown here in green. The dotted red line shows one imaging plane. Fluorescent images are taken at multiple heights, up and down the solid red arrow, to capture more deposition data.

entire deposition. This means that only the brightest value for any particular pixel position in all ten of the images is used. The starting and ending points are set manually for each deposition imaged. A live view of the deposition is viewed and the imaging height is gradually increased and up and down. Since no portion of the deposition is floating above or below the rest of it, the points at which the deposition only dims everywhere in either direction are used as the starting and ending points of the sweep. The maximum intensity projection images are then exported from the Leica imaging software program for analysis.

Grayscale images of depositions left by titanium oxide-laden droplets are taken using a Zeiss Axio Scope microscope in the Nano-Bio Interface Laboratory (NBIL) at RIT. Because the depositions were slightly larger than the field of view of the 10x objective lens, four images were recorded for each deposition. These were stitched together using an open-source MATLAB script, Lilo.m, to produce a higher-resolution, more detailed image than would be possible with the alternative 2.5x objective lens (Fig. 3.6). Stitched images used have a bit depth of 8 and have resolutions of approximately 1600x1200 pixels. The images have less-distinct, light-grey backgrounds and areas of darker shades of grey where particles deposited. Here, the darker regions correspond to areas of higher particle concentration, since thicker depositions allow less light to pass through them.

Once images are collected, they are read into MATLAB and analyzed with a custom code. The code used is detailed in Appendix C. The two types of images are pre-processed differently.

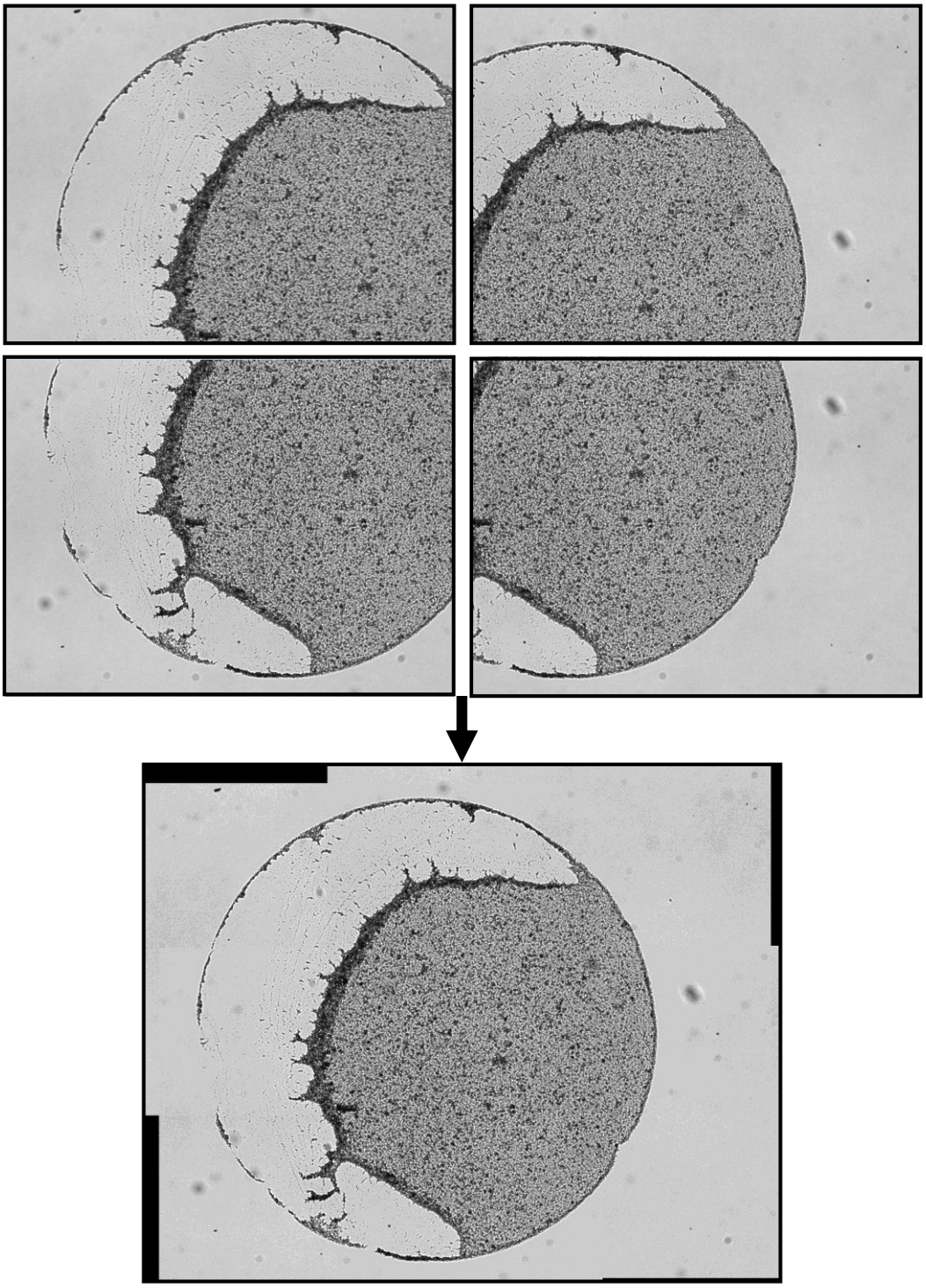

Figure 3.6 Four captured images of titanium oxide depositions can be stitched into a single image for processing. This technique increase the resolution of the image used as compared to using a lower microscope objective strength to capture the entire deposition at once.

Fluorescent images of polystyrene depositions are simply converted to grayscale. Brightfield images of titanium oxide depositions are first inverted so that image intensity corresponds with increased particle concentration. The background is then removed by changing all areas of the image with intensities lower than 80% of the Otsu threshold to black. This leaves the titanium oxide deposition for intensity analysis while eliminating the gray intensities of the background which would skew later results. The resulting image is visually compared to the original to verify that deposition data has not also been deleted and the threshold must be lowered.

A black and white image is then created using the Otsu threshold of the current grayscale image. Ideally, the resulting image is white in regions with deposition and black elsewhere. The image is filtered to remove any white regions smaller than 150 pixels. A convex hull is then fit around the remaining deposition area to form an initial mask. The filtering prevents stray pixels or small foreign debris outside of the deposition from producing a convex hull that poorly fits the deposition area. Using the grayscale image as a reference, the initial mask is then contoured inward to fit the deposition area more closely and form the final mask (Fig. 3.7a). The grayscale image overlaid with the mask perimeter and calculated centroid is saved for later review to ensure the mask matches the deposition.

This mask generating process excels at analyzing fluorescent images where there are primarily large regions of deposition. The titanium oxide-laden droplets tend to leave depositions with sparsely coated regions. The filtering that removes stray pixels for creating the convex hull can also remove these, which results in deleting a portion of the deposition. However, the deposition areas are clearly contained in a highly circular area. To create masks for the titanium oxide depositions, the MATLAB code is modified to detect the deposition circle in the image. An initial circle mask is created using the radius identified for the deposition but increased by 5% to

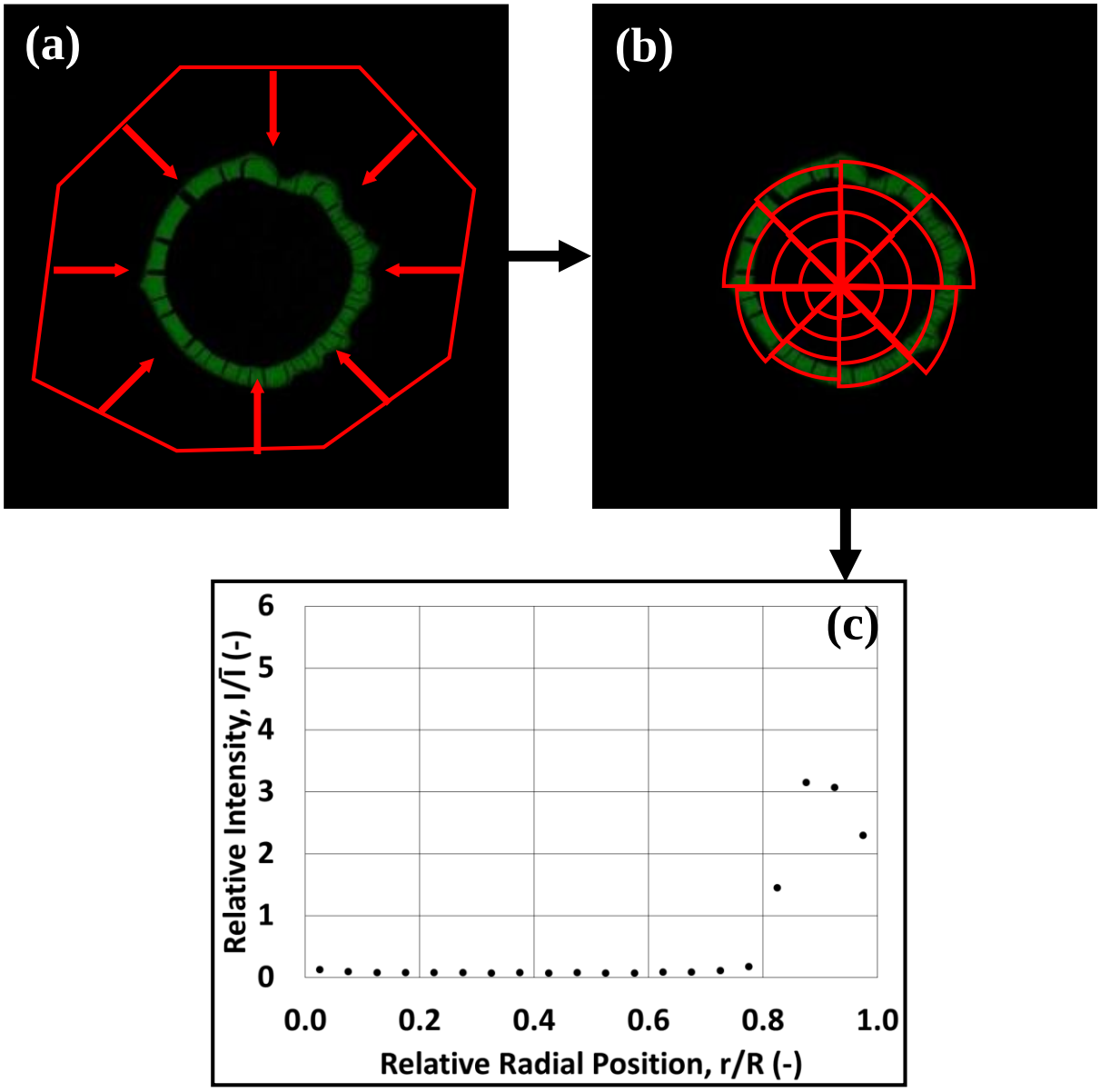

Figure 3.7 The deposition imaging procedure consists of (a) defining the region of interest by contouring an initial convex polygon to fit the deposition pattern, (b) subdividing the region into annular sectors, and then quantifying the intensity in each. Intensities at different azimuthal positions, but the same radial position, are averaged to quantify deposition intensity at that particular radial position. This is repeated for all radial positions to produce (c) radial distribution profiles for each deposition.

include any irregular portions of the deposition protruding from the identified circular region. The circle mask is applied to the black and white image to eliminate all debris outside of the deposition area. A convex hull is then fit around any remaining objects and contoured inward toward the

deposition using the initial grayscale image as a reference to form the final mask.

The masked grayscale image is then divided at the centroid into 20 sectors of equal angles. A mean radius is calculated for each sector based upon the angle and the measured area in each region. The sector regions are further subdivided by 20 circular arcs equally-spaced along the radius to form a total of 400 "annular sector" regions over the deposition (Fig. 3.7b). Image intensity in each is measured. Intensities at the innermost annular sector region in each sector are averaged to determine the mean intensity for the inner 5% of the deposition. This process is repeated radially outward to calculate the mean radial intensity distribution for the deposition (Fig. 3.7c). The final values are normalized relative to the mean intensity of the entire deposition. Distributions from multiple depositions from a single case are averaged and plotted along with three standard deviations for profile comparison between cases.

3.5 Actuation

All actuated trials are performed at a DC voltage of either +160 *V* or -160 *V*. Droplets of DI water were previously observed to exhibit contact angle saturation beyond an actuation signal of 80 *V* [49]. This limit was doubled to ensure the actuation voltage was well into the saturation range. In the event of a deviation in dielectric thickness, the apparent contact angle after the voltage is applied should remain approximately the same value. This allows for results recorded from droplets on different devices to be comparable since they were subjected to similar conditions during evaporation.

Actuation is applied using a three-part control system. The first component is a National Instruments (NI) PXI-5402 signal generator which produces the initial signal. The signal generator has a maximum output of 5 *V*. This is too weak to produce observable contact angle deformation using the device configuration described in Section 3.2. For this reason, the initial low-voltage

signal is sent to the second component, a Trek PZD700A amplifier. Here, the signal is stepped up at a gain of 200 *V/V* and directed to the device electrode. Additionally, a 1/200 *V/V* stepped-down signal is also sent to the third component of the system, an NI PXI-4072 digital multimeter. This is used to monitor the signal used and ensure the applied voltage is correct. The signal generator and digital multimeter are both housed in an NI PXI-1033 chassis during operation. To complete the circuit, a ground wire is inserted into the top of the droplet. The wire used is typically made of tungsten and is 22 μm in diameter. Earlier trials utilized a nichrome wire 80 μm in diameter.

4.0 RESULTS AND DISCUSSION

Colloidal deposition is critical in a variety of applications that involve the deposition of a wide array of materials, including proteins for biopreservation, DNA and polystyrene particles in microarray testing, and metal particles in inkjet printing. This work characterizes the effects of particle size (Sec. 4.1) and particle type (Sec. 4.2) on the contact line dynamics and colloidal transport of evaporating particle-laden droplets. The experimental conditions for each set of trials performed are summarized in Appendix D. Particles tested were selected based on their potential use in these applications. Side-view images of particle-laden droplets are recorded and used to study the transient droplet profile behavior. The apparent contact angles and diameters of the droplet over time are then calculated from the images and plotted to observe the contact line dynamics throughout the duration of evaporation. Final deposition patterns are imaged and then analyzed using custom MATLAB script to quantify the intensity distribution, and by proxy the particle distribution, left by each droplet.

The application of electric fields is a promising means for influencing colloidal transport in evaporating particle-laden droplets. By manipulating the magnitude and polarity of the applied field, different forces can be applied to the droplet and suspended particles. This, in turn, can direct particles towards different locations as they deposit. Both AC [37,38,47] and DC [44] electric fields have previously been used to manipulate colloidal transport in particle-laden droplets. In the body of literature examined during this investigation, no distinctions are made regarding the effects of DC polarity on electrowetting effects experienced by an actuated droplet. Preliminary results examining the effects of DC actuation polarity are presented in Section 4.3. Transient behaviors of actuated droplets of different particle concentrations are quantitatively

Table 4.1: Contact angles and pinning forces of droplets seeded with different polystyrene sizes.

Droplet Type	Initial Angle	Receding Angle	Pinning Force
DI Water	89°	73°	19.8 *mN/m*
25 *nm* Polystyrene	88°	73°	18.5 *mN/m*
63 *nm* Polystyrene	91°	76°	18.7 *mN/m*
1.1 μm Polystyrene	92°	76°	19.9 *mN/m*

compared. The resultant deposition patterns are also qualitatively discussed. The experimental conditions of all sets of trials performed during this study are also summarized in Appendix D.

4.1 Effects of Particle Size

In order to understand the effects of particle size, droplets seeded with polystyrene particles of different sizes were evaporated on SU-8 photoresist. Particles were 25 *nm*, 63 *nm*, or 1.1 μm in diameter. Deionized (DI) water was used as the solvent for all droplets. Each was seeded at a particle concentration of 0.05% by volume. A fourth set of control trials consisted of DI water droplets without particles to observe the impact of particle presence on transient evaporative behavior. Deposited droplet volumes were 1 μL. Droplets were not exposed to external electric fields and did not have ground wires inserted into them during evaporation. A minimum of five trials were performed for each case.

The contact angle and diameter evolutions for the four cases are presented in Figure 4.1. Mean values and three standard deviations are shown in black and red, respectively. The dashed blue lines in Figures 4.1d, 4.1f, and 4.1h indicate the diameters of the final deposition patterns. In each case, clear evaporation regimes are observable. At different times, droplets exhibited the constant contact diameter (CCD), constant contact angle (CCA), and mixed regimes. Overall, the transient behaviors of each case appear largely similar, regardless of particle presence or size. All start at initial contact angles of approximately 90° (Table 4.1). Droplets are initially pinned in place on the surface, and their contact angles decrease for the first 30% of evaporation. This

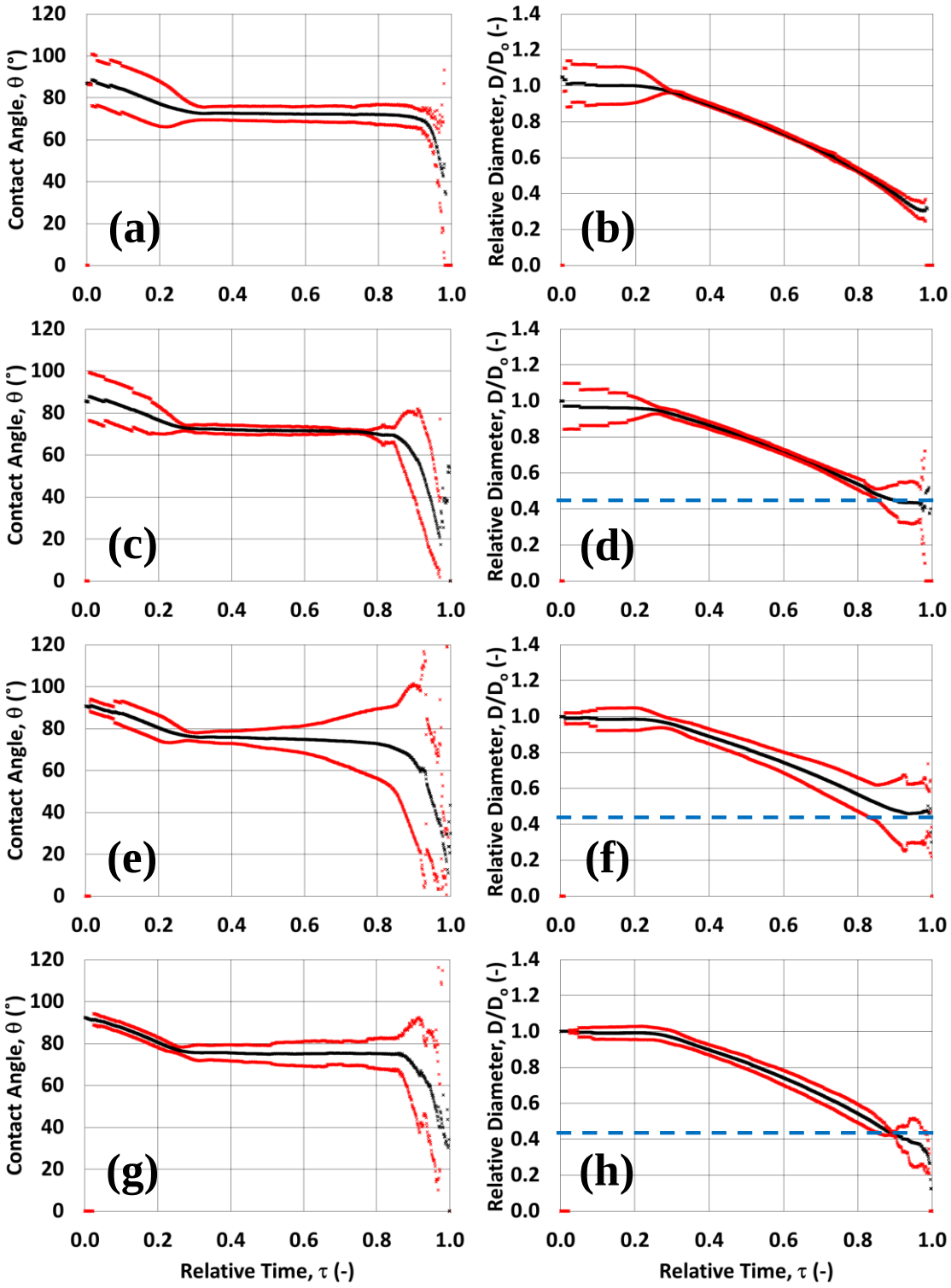

Figure 4.1 Transient droplet profiles during the evaporation of (a,b) DI water droplets and DI water droplets seeded with (c,d) 25 *nm*, (e,f) 63 *nm*, and (g,h) 1.1 *μm* polystyrene particles. Mean values are shown in black, and three standard deviations above and below are shown in red. Dotted blue lines indicate the mean final diameter of depositions left after evaporation.

continues until the droplets reach their receding contact angle. In all cases, this is observed to be approximately 75°. At this point, the contact lines begin to recede and the droplet transitions into the CCA regime. For the particle-laden droplets, this lasts through 85% of the evaporation time. In the DI water control case, it extends slightly longer until approximately 95% of the total evaporation time.

For the remainder of evaporation in each case, the droplets seeded with 25 *nm* and 63 *nm* particles return to a CCD evaporation regime where the contact line repins. This repinning may be the result of the increased particle concentration at the contact line. Concentrated particles can start to form a ring of deposition which can keep the droplet pinned [50]. The 1.1 μm and DI water cases instead exhibit a mixed evaporation regime where both contact angle and diameter reduce. The DI water droplet case does not have particles that can aid in repinning the droplet to enter a CCD regime. This may also be why the CCA regime extends longer. As for the 1.1 μm case, the particles may not collect at the periphery and increase in concentration enough to cause repinning. This particle-induced pinning effect can be influenced by particle size, and larger particles can migrate toward the droplet center instead of toward the periphery [28].

Since the particle-laden droplets and DI water droplets recede at the same angle, it is likely that particle concentrations at the periphery are not high enough 30% into the evaporation time to jam the contact line and impede slipping. This is consistent with previous work suggesting it is more difficult for particle jamming to impede contact line dynamics on hydrophobic surfaces [51,52]. The magnitude of the pinning force when the droplets slip in each case can be calculated as,

$$dF = \gamma_{lv}\left(\cos\theta_r - \cos\theta_{eq}\right), \tag{4.1}$$

where dF is the pinning force per unit length acting on the contact line, γ_{lv} is the surface tension

along the liquid-vapor interface, θ_r is the receding contact angle, and θ_{eq} is the equilibrium contact angle [31]. This equation is derived by adding an additional pinning force into the Young equation (Eq. 3.2) which resists the inward motion of the contact line as the droplet evaporates. Taking the surface tension of water to be 72 *mN/m*, the pinning forces for each case can be calculated to be as shown in Table 4.1. Here, the initial contact angle was taken to be the equilibrium contact angle, θ_{eq} [31]. In all cases, the pinning force peaks at approximately 19 *mN/m*. No clear trend is evident with increasing particle size, and all magnitudes are within 8% of each other. This indicates that particle presence, regardless of size, does not have a significant affect the depinning threshold in these cases.

Representative images and fluorescence intensity distributions of depositions left by 25 *nm*, 63 *nm*, and 1.1 μm particles are shown in Figure 4.2. All patterns have outer diameters approximately the same size, 650 μm. Despite exhibiting similar transient behaviors (Fig. 4.1), the deposition distributions in these areas are quite different. The 25 *nm* particles leave a cracked coffee-ring pattern similar to the dried colloidal microsphere patterns seen by Deegan *et al*. [23] (Fig. 4.2a). The inner and outer diameters of the coffee-ring are clearly defined with little fluorescence intensity toward the center of the droplet. The intensities in these bands are approximately 4.7 times the mean intensity. The deposition patterns left by the 1.1 μm particles are much more uniform (Fig. 4.2c). Intensity at any radial position only ranges between 0.65 and 1.2 times the mean intensity. The 63 *nm* particles also leave coffee-ring patterns (Fig. 4.2b). However, the inner diameters of the deposition bands are less distinct and fluorescence intensity more gradually fades toward the center of the deposition area. The peak band intensity in this case is only 2.7 times the mean intensity. These results suggest that while particle size does not impact the final diameter of the deposition, it can dramatically change the final deposition distribution

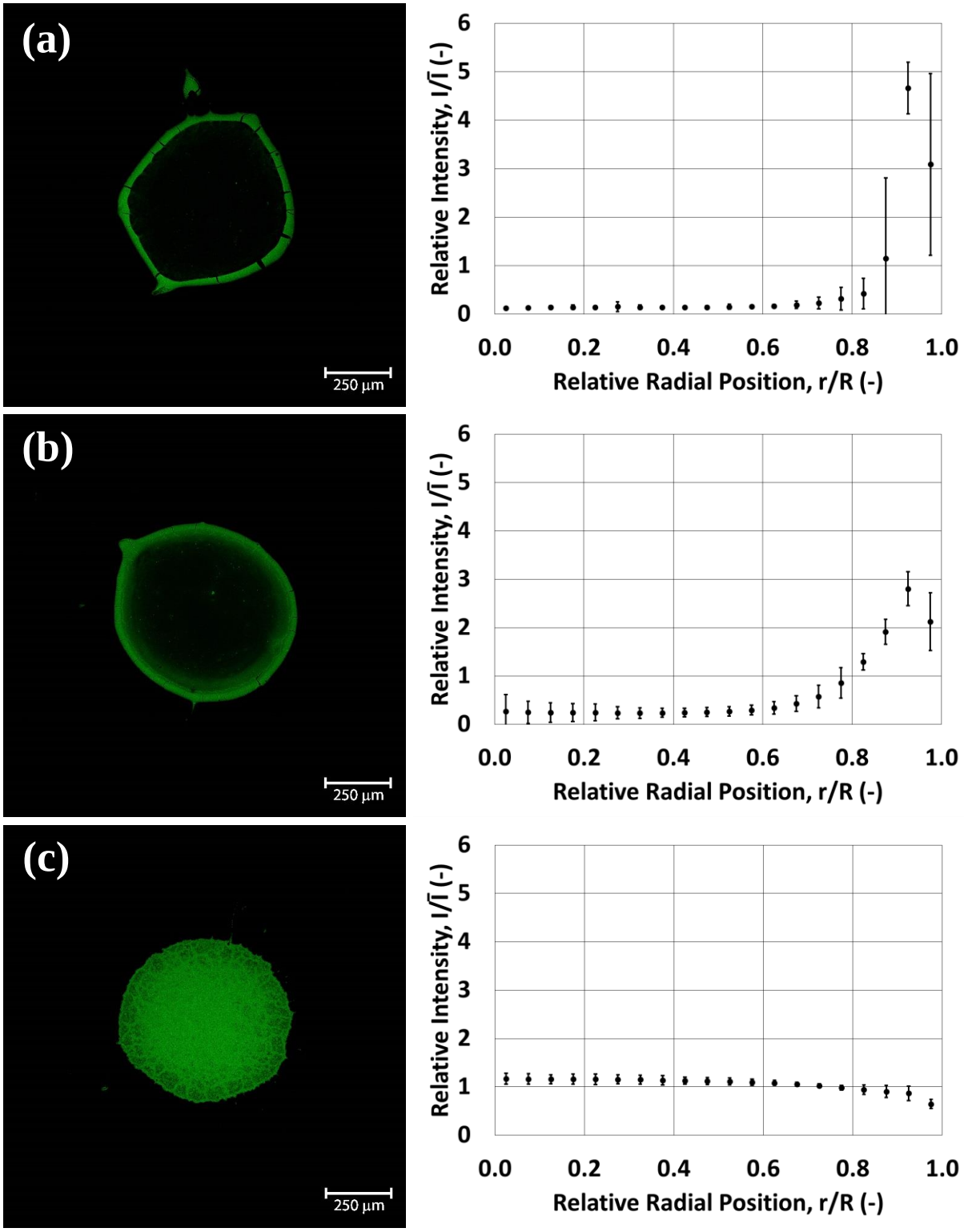

Figure 4.2 Representative depositions patterns and particle distribution profiles left after evaporation of DI water droplet seeded with (a) 25 *nm*, (b) 63 *nm*, and (c) 1.1 μm polystyrene particles. Error bars span three standard deviations above and below the mean values.

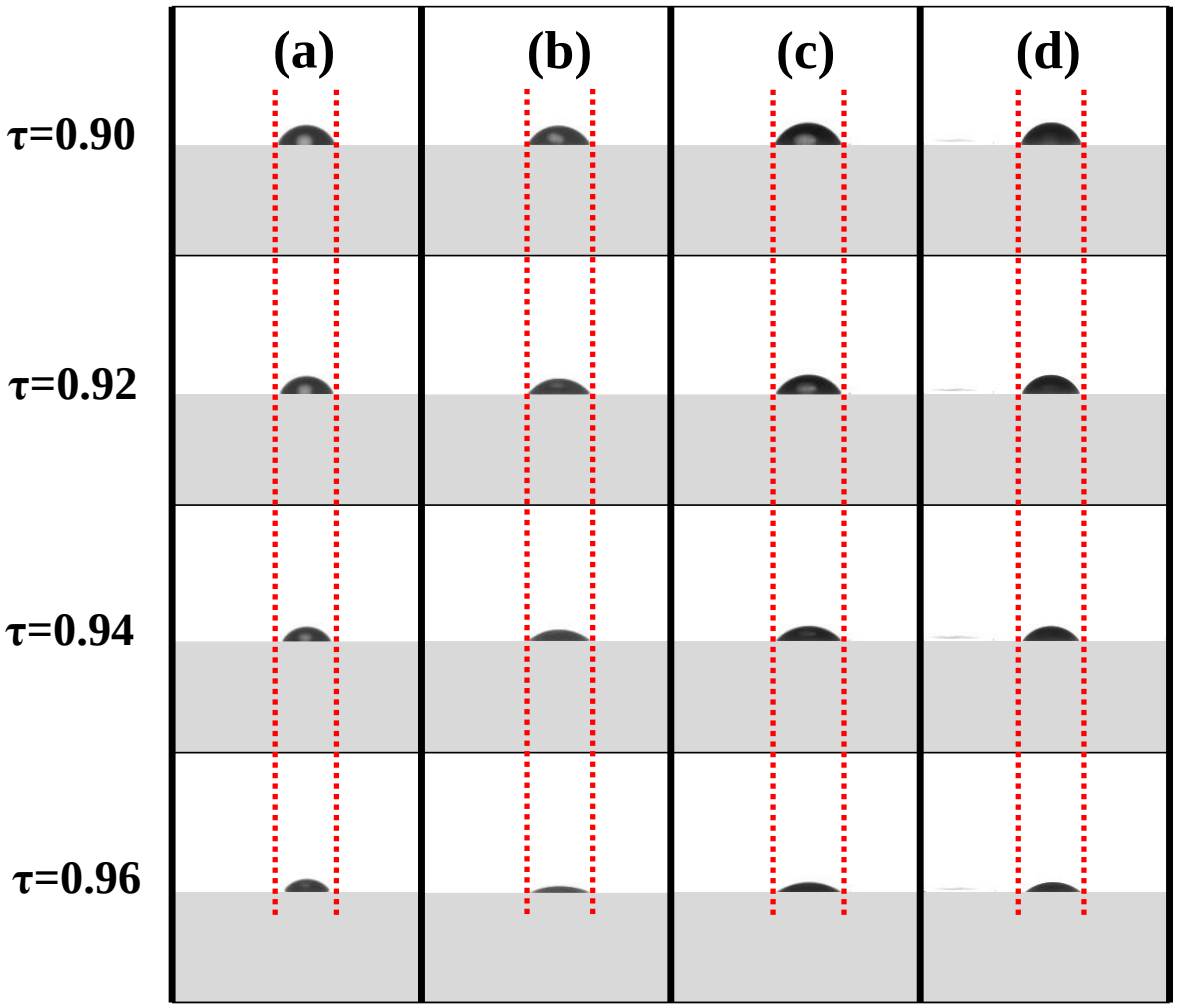

Figure 4.3 Representative profile images of evaporating droplets of (a) pure DI water and DI water seeded with (b) 25 *nm*, (c) 63 *nm*, and (d) 1.1 *μm* polystyrene particles starting 90% into evaporation. In (b) and (c), the droplet appears to remain pinned.

pattern.

Late-stage contact line pinning [53,54] seems to account for the differences in the deposition patterns observed with particle size. As the droplet evaporates, particle concentration at the contact line increases, and the contact line is predicted to repin once the concentration at the contact line reaches a linear density of 10% [54]. Evidence of late-stage pinning in the 25 *nm* and 63 *nm* particle cases can be observed in the transient behaviors. In the final 10% of the evaporation, the contact diameters remain relatively constant (Fig. 4.3). This indicates the droplet is pinned in

its final moments. This pinned contact line means that the radially outward evaporative flow is active and can work to carry particles toward the outer periphery to form a coffee-ring deposition pattern. Interestingly, the evolution of the contact diameter for the 1.1 μm particles more closely resembles that of the particle-free droplet where the contact diameter continues to decrease in the final 10% of evaporation. This supports the idea that droplets seeded with larger particles are less likely to exhibit late-stage pinning.

Results from Figures 4.1 and 4.2 suggest that larger particles are more likely to sink to the substrate than to be swept to the contact line. Stokes, or terminal, velocity in a stagnant flow, U_S, can be determined by equating the drag on the particle to the gravitational force as shown,

$$U_S = \frac{2}{9}\frac{(p_p - p_f)}{\mu} g R_p^2, \tag{4.2}$$

where, g is the acceleration due to gravity, μ is the dynamic viscosity of the fluid, R_p is the radius of the particle, and ρ_p and ρ_f are the densities of the particle and fluid, respectively. Since the initial droplet height and evaporation time are known, a vertical Strouhal number, Sr_z, can be defined as,

$$Sr_z = \frac{t_f}{H/U_s} = \frac{2t_f}{9H}\frac{(p_p - p_f)}{\mu} g R_p^2, \tag{4.3}$$

where, H is the initial height of the droplet and t_f is the total evaporation time.

While the Strouhal number is often used to characterize colloidal transport in evaporating droplets, it is typically defined in the radial direction to compare evaporation time to the time required for the particle to be transported to the pinned contact line [28]. This vertical Strouhal parameter estimates the ratio of drying time to the time required for a particle to settle to the surface at terminal velocity. A larger value of Sr_z implies that the particle is more likely to settle to the substrate due to gravitational effects. By carrying particles toward the substrate, the gravitational forces may delay or prevent the concentrating of particles at the periphery which can lead to ring formation and droplet repinning during evaporation [50]. When the evaporative flow is

diminished, as in the case of a moving contact line, these gravitational effects may play a more significant role in colloidal transport.

It should be noted that this vertical version of the Strouhal analysis makes two assumptions that are not considered in more typical radial Strouhal analyses. First, particles are assumed to accelerate quickly to their Stokes velocity. Particles in fluids experience a gravitational acceleration up to their Stokes velocity,

$$U_S = k(1 - e^{-t_f/\tau_S}), \tag{4.4}$$

where k is a proportionality constant and τ_S is the Stokes velocity time constant,

$$\tau = \frac{m_p}{6\pi\mu R_p}, \tag{4.5}$$

where m_p is the mass of a particle. Even for the largest particles, the time constant much less than one second. Thus, the exponential term in Equation 4.4 rapidly approaches zero. This means the particles rapidly approach their terminal velocity and this assumption is reasonable.

Second, the droplet height is assumed to be fixed. During experimentation, the heights were observed to decrease over time. This is implied in the results shown in Figure 4.2 where contact angles and diameters both decreased over the course of evaporation. The height of the droplet must also have decreased. The reduction in droplet height is unavoidable, and it should be considered that this will aid in carrying particles downward toward the surface faster.

Since Sr_z is proportional to R_p^2, it decreases rapidly as particle radius diminishes. In the cases examined here, Sr_z for the 1.1 μm particles (0.043) is more than 2000 times greater than for the 25 *nm* particles (0.000020) and more than 300 times greater than for the 63 *nm* particles (0.00014). This suggests that gravitational effects are more important for larger particles. As such, a larger percentage of the 1.1 μm particles would settle to the substrate than in the 25 *nm* or 63 *nm* cases. This may contribute to a lower concentration of particles at the contact line for the larger

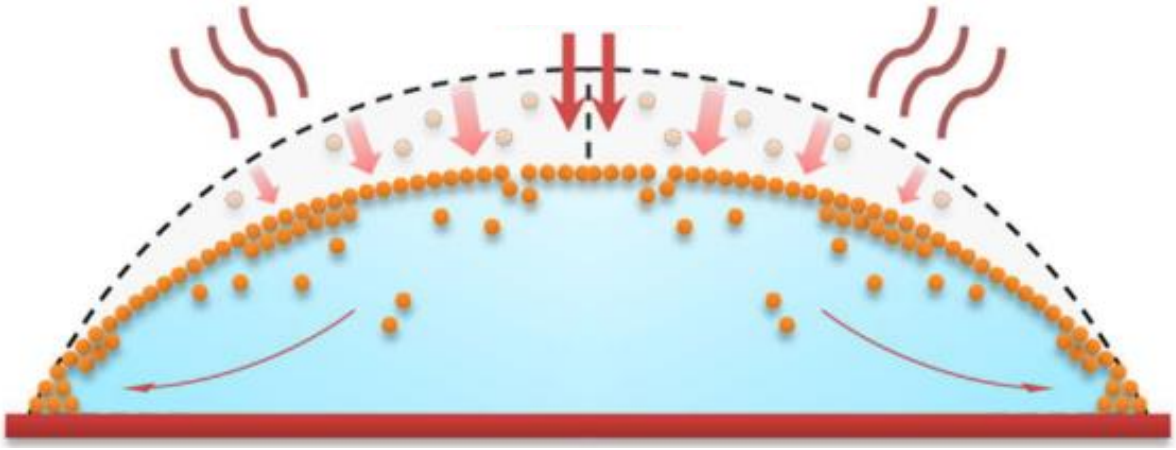

Figure 4.4 If the interface of an evaporating droplet can collapse faster than particles within the droplet can diffuse away from the interface, the particles can be captured by the collapsing interface rather than be swept toward the periphery by the evaporative flow [55].

particles, which could delay late-stage pinning. However, in all cases the magnitude of the vertical Strouhal number is less than 1, so the droplet evaporates faster than particles reach the surface. In the case of the 1.1 μm particles, because the time for a particle to reach the surface is still within two orders of magnitude of the evaporation time, gravitational effects may still have some non-negligible influence on deposition.

The deposition distribution differences may also be due to differences in the diffusion rates of the different sizes of polystyrene particles. As a particle-laden droplet evaporates, the collapsing droplet interface can collect the suspended particles across the interface if it collapses faster than the particles can diffuse away [55] (Fig. 4.4). The speeds of the collapsing interface and particle diffusion can be compared to quantify this capture effect. The collapsing interface speed, v_i, can be calculated as,

$$v_i = H/t_f. \tag{4.6}$$

Equation 4.6 approximates the speed as constant over the duration of evaporation. Droplets

containing all three sizes of polystyrene particles exhibited similar transient interface shapes, and correspondingly had similar interface speeds of approximately 1 $\mu m/s$. The particle diffusion distance, x_p, within an evaporating droplet can be calculated as,

$$x_p = 2\sqrt{k_D t/\pi}, \tag{4.7}$$

where k_D is the diffusion constant and t is the evaporation time. A particle diffusion speed, v_p, in units of distance per second can be approximated from Equation 4.7 by using a value of 1 second for t and approximating k_D from the Stokes-Einstein relation,

$$k_D = \frac{k_B T}{6\pi\mu R_p}, \tag{4.8}$$

where k_B is the Boltzmann constant and T is the temperature of the droplet. The 25 *nm*, 63 *nm*, and 1.1 μm particles have diffusion speeds of approximately 4.9 $\mu m/s$, 3.1 $\mu m/s$, and 0.73 $\mu m/s$, respectively. This suggests that the two smaller particle sizes can diffuse away from the collapsing interface during evaporation. This would allow them to be swept outward toward the periphery to enhance contact line pinning as they concentrate and form rings. The interface collapses approximately 1.4 times as fast as the 1.1 μm particles diffuse. This would result in a collection of particles over the droplet interface as the droplet evaporates. This mechanism may have a greater influence on the formation of the more uniform deposition patterns left by the 1.1 μm polystyrene-laden droplets.

4.2 Effects of Particle Type

In order to understand the effect of the type of particle selected, droplets seeded with polystyrene and titanium oxide particles of similar sizes were evaporated on SU-8 photoresist. Polystyrene particles were 25 *nm* in diameter, while the titanium oxide particles were 21 *nm* in diameter. In these experiments, droplets were seeded at a lower particle concentration of 0.02% by volume. At a concentration of 0.05%, titanium oxide particles tended to begin falling out of

suspension and clumping within ones of minutes after sonication. Deposited droplet volumes were 1 μL. Droplets were not exposed to external electric fields and did not have ground wires inserted into them during evaporation. A minimum of five trials were performed for each case. The results from these two cases were compared to the DI water case from the particle size study as a control to observe the impact of particle selection on transient evaporative behavior.

The contact angle and diameter evolutions for the three cases are presented in Figure 4.5. Mean values and three standard deviations are shown in black and red, respectively. The dashed blue lines in Figures 4.5d and 4.5f indicate the diameters of the final deposition patterns. All droplets exhibit an apparent contact angle of approximately 90° when evaporation begins (Table 4.2). Further, all droplets remain pinned for the first 30% of the total evaporation time. In this constant contact diameter regime, the contact angle and height decrease with droplet volume. Beyond this point, the DI water and polystyrene-laden droplets exhibit very similar behaviors, while the titanium oxide-laden droplets deviate significantly.

From approximately 30% to 90%, the DI water and polystyrene-laden droplets transition to a CCA regime. In both cases, the contact angle reduction halts at a receding contact angle of approximately 75°. The droplets then begin steadily reducing in diameter, as well as height. The diameters appear to pin once more near the end of evaporation from 90% to 95%. Beyond this point, measurements are erratic or zero. This is due to limitations of the Ramé-Hart goniometry system when measuring small droplet volumes or angles below 20° [33].

The titanium oxide-laden droplets remain pinned until approximately 60% of the total evaporation time. At this point, the angle reaches the receding contact angle limit of approximately 44°. The droplet then enters a regime of repeated slip-stick behavior [19,38,44] from 60% to 80%. This is evidenced by the saw-tooth pattern in the contact angle (Fig. 4.5e) and the step-down

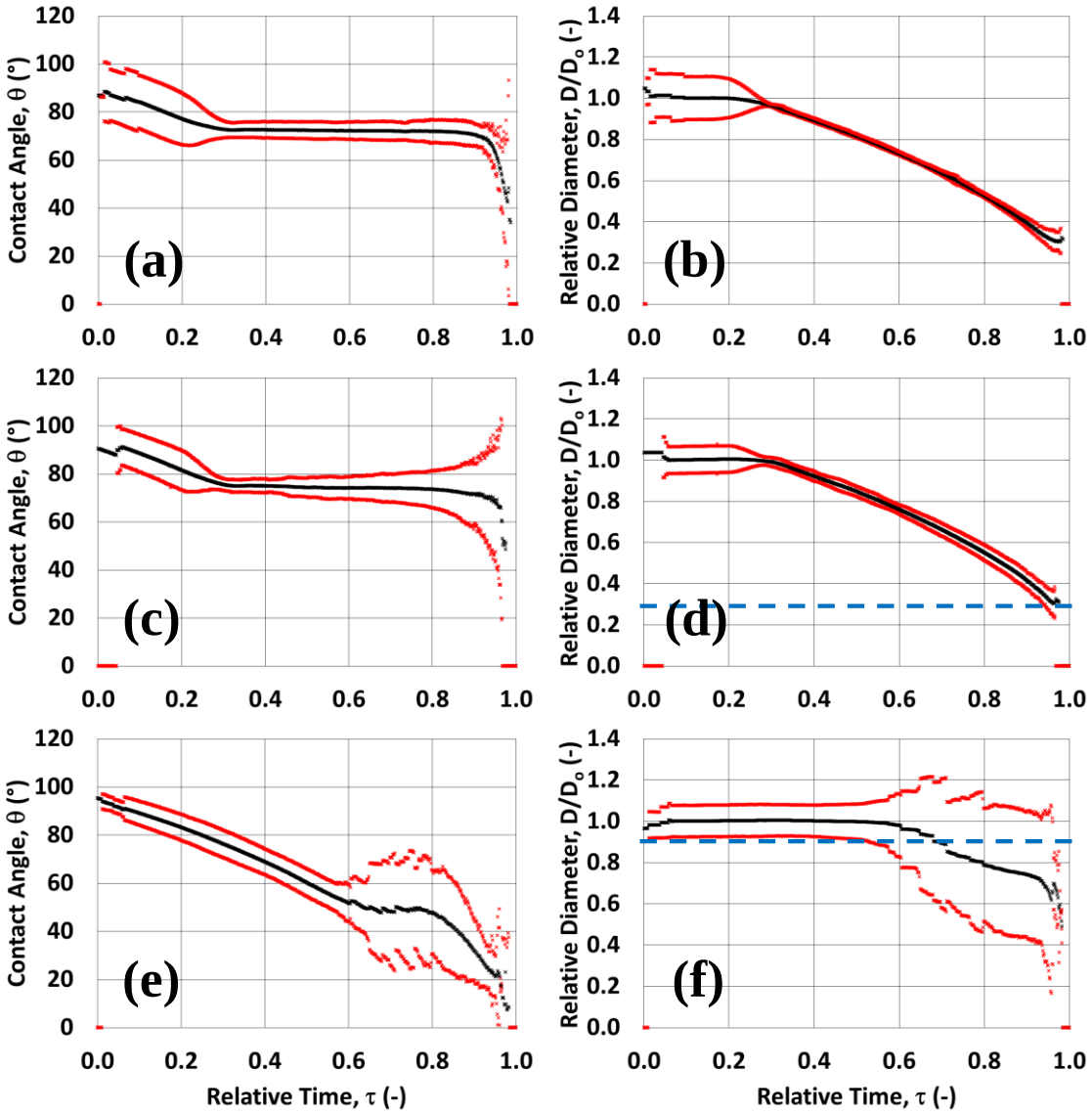

Figure 4.5 Transient droplet profiles during the evaporation of (a,b) DI water droplets and DI water droplets seeded with (c,d) 25 *nm* polystyrene particles and (e,f) 21 *nm* titanium oxide particles. Mean values are shown in black, and three standard deviations above and below are shown in red. Dotted blue lines indicate the mean final diameter of depositions left after evaporation.

pattern in the diameter (Fig. 4.5f). The results of one representative trial are presented in Figure 4.6. The slip-stick behavior is more readily observed in the individual trial plots rather than the composite plot (Fig. 4.5e,f). The droplets then transition into a mixed regime for much of the remainder of evaporation. Again, the measurements in the final 5% are erratic or zero due to errors

Table 4.2: Contact angles and pinning forces of droplets seeded with different particle types.

Droplet Type	Initial Angle	Receding Angle	Pinning Force
DI Water	89°	73°	19.8 *mN/m*
Polystyrene	92°	75°	21.1 *mN/m*
Titanium Oxide	95°	44°	58.1 *mN/m*

in the measuring system at such small droplet sizes.

The peak pinning forces at the end of the initial CCD regime can again be calculated for each case using Equation 4.1. The resulting values are shown in Table 4.2. The pinning force for the polystyrene-laden droplets is similar in magnitude to the particle-free case at approximately 20 *mN/m*. The titanium-oxide laden droplets experience much higher pinning forces. They are calculated to be nearly triple that of polystyrene-laden droplets at 58 *mN/m*.

Representative polystyrene-laden and titanium oxide-laden droplet depositions and deposition distributions are shown in Figure 4.7. Similar depositions are observed in the other trials of each case. Though all droplets used have an initial diameter of approximately 1.6 *mm*, the polystyrene-laden droplets produce much smaller final depositions, approximately 450 μm in diameter, as compared to the titanium oxide-laden droplets, approximately 1400 μm in diameter.

The polystyrene depositions take a distinct coffee-ring form. The large majority of particles are deposited at the outer periphery where the droplets pin near the end of evaporation. The maximum intensity occurs at the periphery of the deposition where it is 2.65 times the mean. Minimal deposition is present towards the centers. Through the inner 60% of the depositions, intensity is only a fraction, less than 0.2, of the mean intensity. The polystyrene depositions also exhibit distinct cracking similar to polymer depositions previously observed by Deegan *et al*. [23,56].

The titanium oxide-laden droplets leave a more complex deposition distribution. Two distinct coffee-rings are observable. At the outer periphery, a thinner ring of titanium oxide

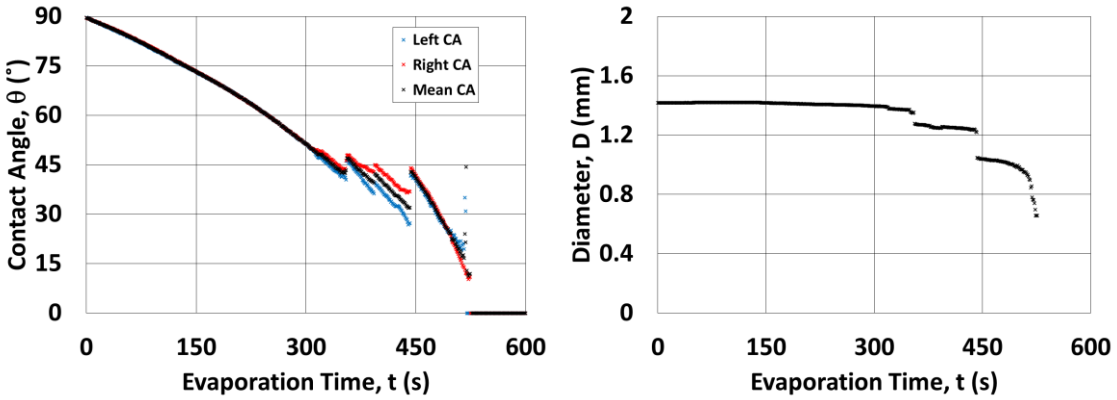

Figure 4.6 Representative transient profile of an evaporating titanium oxide-laden droplet. After the initial CCD region, the droplet slips and sticks several times through the rest of evaporation.

outlines the deposition area where the droplets repinned and deposited material near the end of evaporation. A thicker partial ring of titanium oxide divides the deposition areas into two regions. In the first, smaller region, a number of faint coffee rings are visible where a portion of the droplet appears to have slipped inward a number of times (Fig. 4.7b). Overall, however, there is little total deposition in this region. In the second, larger region, particle deposition is more uniform. Intensity hold at approximately 1.45 times the mean intensity through the inner 50% of the entire deposition area.

This pattern is unusual considering the transient behavior of the titanium oxide-laden droplets. In these cases, the contact line was initially pinned for the twice the fraction of evaporation as the polystyrene-laden droplets. This suggests that the evaporative flow carrying particles to the periphery is active for more of evaporation in the titanium oxide-laden droplet case. Interestingly, a significant amount of the titanium oxide particles are deposited toward the center of the deposition. The differences in colloidal transport between the two particle-laden droplet cases suggest that an additional effect may be at play influencing particle motion.

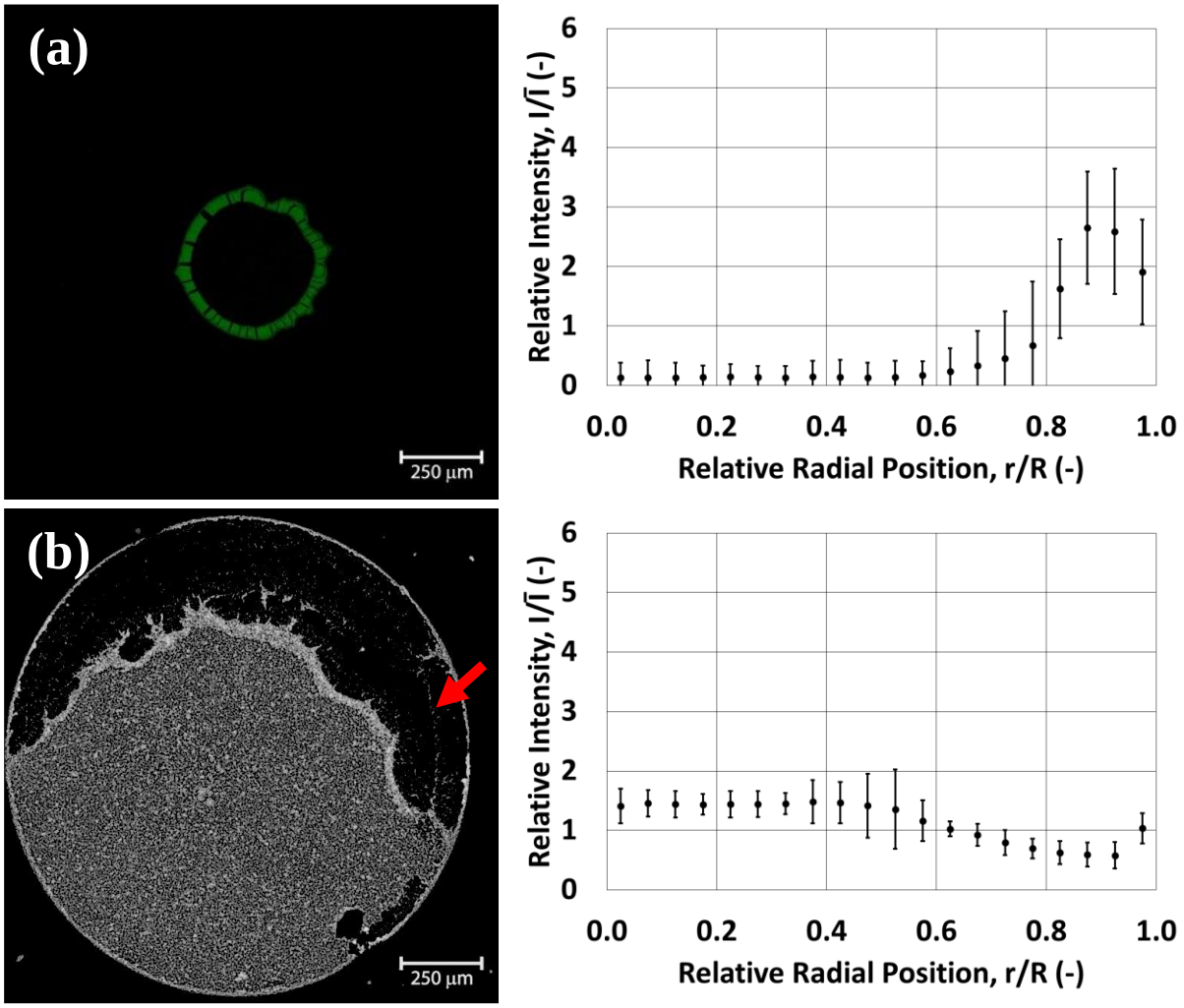

Figure 4.7 Representative depositions patterns and particle distribution profiles left after evaporation of DI water droplet seeded with (a) 25 *nm* polystyrene particles and (b) 21 *nm* titanium oxide particles. Error bars span three standard deviations above and below the mean values. The representative titanium oxide image has been inverted and has had its background removed. The red arrow points toward what appears to be one of several faint deposition rings.

While both types of particle-laden droplet were similar in terms of particle size and concentration, one significant difference between them is the density of the particles used. The polystyrene particles have a density of approximately 1.055 g/cm^3, while the titanium oxide particles have a density of approximately 4.26 g/cm^3, as reported by their manufacturers. In order for a coffee ring to form, an outward evaporative flow must dominate within the droplet as it dries

[22]. However, gravitational forces also act upon the particles and could cause particles to settle to the substrate.

The terminal velocity of a spherical particle falling in a fluid is proportional to the difference in density between the particle and the surrounding fluid as shown in Equation 4.2. Taking the density of the deionized water to be 0.997 g/cm^3, the density difference of the polystyrene particles is 0.058 g/cm^3. This means the particles are close to neutrally buoyant. This small value may explain why the addition of the polystyrene particles had no significant impact on the transient droplet behavior (Fig. 4.5a-d). Meanwhile, titanium dioxide has a density difference of 3.263 g/cm^3. Simply comparing the density differences, the titanium oxide particles experience a downward terminal velocity approximately 56 times greater than that of the polystyrene particles.

Using the same analysis presented in Section 4.1, a vertical Strouhal number can again be calculated for each case using Equation 4.3. Based on the parameters of the trials conducted, the polystyrene particles have an Sr_z value of 0.00022 while the titanium oxide particles have a value nearly 33 times larger at 0.00073. Because both values are much smaller than 1, by the time a particle settles in either case, the droplet has likely evaporated. This suggests that gravitational effects are not responsible for the differences in deposition patterns observed in these cases.

Additionally, interface capture is likely not contributing to the uniformity of the titanium oxide depositions. Since both types of particles have similar sizes and the evaporation times of both types of droplet do not vary substantially, interface capture likely has a similar effect in both cases. Computing the interface speeds using Equation 4.6, the polystyrene-laden droplets had speeds of approximately 1 $\mu m/s$ similar to the higher concentration polystyrene-laden droplets analyzed in Section 4.1. The titanium oxide-laden droplets evaporated slightly faster than the

polystyrene-laden droplets and had interface speeds of approximately 1.2 $\mu m/s$. Using Equations 4.7 and 4.8 to calculate the particle diffusion speeds shows that both types of particles diffuse at rates of approximately 5 $\mu m/s$. Since the diffusion rates are several times higher than the interface speeds, particles likely do not accumulate over the interfaces throughout the course of evaporation in either case.

Another effect must be at play causing the different behaviors exhibited by the two different particle-laden cases. An effect that concentrates particles at the periphery more quickly in the titanium oxide case than the polystyrene case could produce the prolonged pinning observed [50] (Fig. 4.5). If the effect collects particles more quickly across all of the droplet-substrate interface and not just at the contact line, it could also produce the uniform regions observed in the final titanium oxide depositions (Fig. 4.7). One possibility is that differences in the electrical properties of the two particles are contributing to the behavioral differences. These properties can influence interactions between the particles and between individual particles and the photoresist surface [36]. Further investigation quantifying the DLVO forces in these cases is necessary to understand their role in droplet evaporation and colloidal transport.

4.3 Effects of Actuation Polarity

In order to begin characterizing the effects of voltage polarity, DI water droplets were deposited and evaporated on SU-8 photoresist. Droplets were exposed to external DC electric fields of either +160 V or -160 V. Tungsten ground wires 22 μm in diameter were used to ground the droplets. A control set of unactuated droplets was also tested. While no voltage was applied, a similar ground wire was still inserted into each control droplet during evaporation. Deposited droplet volumes were 1 μL in volume. A minimum of five trials were performed for each case. Transient profile behaviors were then compared across the three cases.

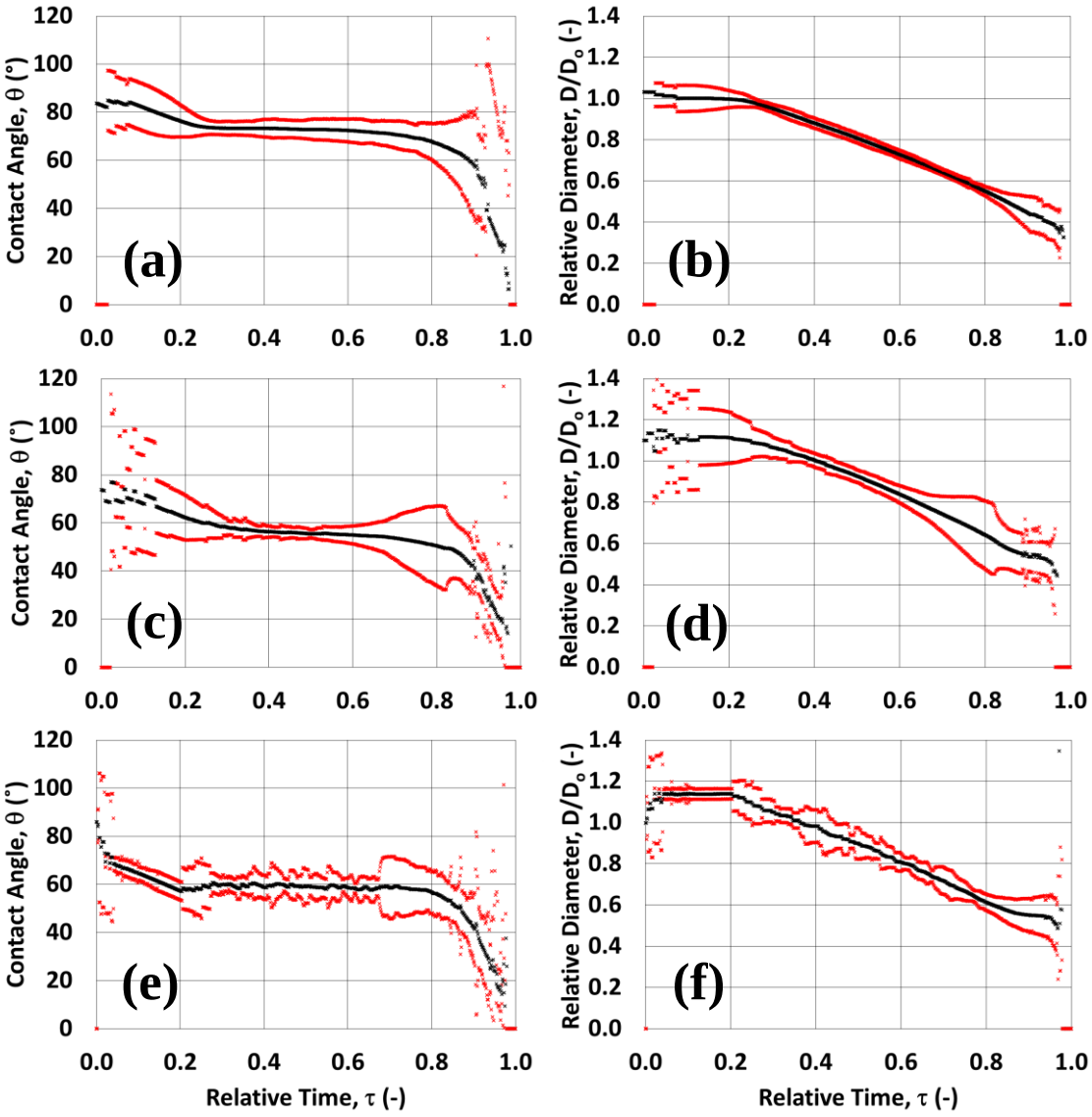

Figure 4.8 Transient droplet profiles during the evaporation of (a,b) unactuated DI water droplets and DI water droplets subjected to (c,d) +160 *V* DC and (e,f) -160 *V* DC. Mean values are shown in black, and three standard deviations above and below are shown in red. All droplets had a ground wire inserted into them during evaporation.

Contact angle and diameter data for the actuated DI water droplet cases and unactuated control case are presented in Figure 4.8. The unactuated control case with the ground wire exhibits behavior very similar to that of the unactuated DI water droplets without wires shown in Figures 4.1a and 4.1b and repeated in Figures 4.5a and 4.5b. Unactuated droplets initially exhibit a contact

Table 4.3: Contact angles and pinning forces of DI water droplets under different actuations.

Droplet Type	Initial Angle	Receding Angle	Pinning Force
Unactuated	85°	74°	13.6 *mN/m*
+160 *V*	70°	55°	16.7 *mN/m*
-160 *V*	69°	58°	12.4 *mN/m*

angle of approximately 85°. They remain pinned for the first 30% of evaporation in a CCD regime until reaching a receding contact angle of 74°. The droplets then slip and recede in a CCA regime until approximately 80% of the total evaporation time. They then exhibit a mixed regime for the remainder of evaporation. The slight reduction in initial contact angle compared to DI water droplets evaporated without a wire may be due to evaporation occurring during the time it takes evaporation occurring during the time it takes to insert the wire into the droplet. This may affect all actuated cases as well.

In the actuated DI water droplet cases, contact angles close to the unactuated initial contact angle are captured during the time period between the start of profile imaging and the start of actuation. The droplets then exhibit initial actuated contact angles of approximately 70° (Table 4.3). Both positively and negatively actuated droplets initially pin. They recede in a CCD regime for approximately the first 20% of evaporation until reaching a receding contact angle of approximately 55°. This reduction in receding contact angle is characteristic of actuated droplets [29]. After this point, the droplets in both cases depin, and the two cases recede differently until 80% through the evaporation time. The positively actuated droplets recede in a CCA regime somewhat like the unactuated DI water droplets. Meanwhile, the negatively actuated droplets exhibit slip-stick behavior [19,38,44]. Through the final 20% of evaporation, both sets of actuated droplets exhibit late-stage pinning.

The two distinctly different means of evaporating from 20% to 80% of the total evaporation time exhibited in these trials is unusual. As shown in Equation 1.3, the electrowetting effects

manipulating the droplet contact line are driven by the square of the voltage magnitude. Thus, polarity should not be a factor. This observed deviation suggests either that the electrowetting effects should depend on polarity or that the voltage is changing how the droplet interacts with the surface by effect other than electrowetting. The latter is more likely, and further investigation into the electrical characteristics of the droplets should be performed.

The pinning force in the unactuated case with an inserted wire can be calculated in the previous two studies to be 13.6 *mN/m* (Eq. 4.1). This is approximately 30% smaller than in similar droplets without inserted wires (Tables 4.1 and 4.2). Again, due to the time it takes to insert the wire into the droplet, some evaporation may have occurred before the profile imaging began. This would result in a smaller initial angle and a correspondingly smaller calculated pinning force. The wire may also have some unknown effect on the pinning experienced by the droplet.

The pinning forces in the actuated cases can be calculated as,

$$dF_a = \gamma_{lv}\left(\cos\theta_{a,r} - \cos\theta_{a,eq}\right), \tag{4.9}$$

where dF_a is the pinning force per unit length acting on the actuated contact line, $\theta_{a,r}$ is that actuated receding contact angle, and $\theta_{a,eq}$ is the actuated equilibrium contact angle. This equation is derived similarly to Equation 4.1, but the electrowetting force applied during actuation has been included. The pinning force of the positively and negatively actuated DI water droplets can then be calculated to be 16.7 *mN/m* and 12.4 *mN/m*, respectively.

To characterize the effects of voltage polarity further, droplets seeded with 25 *nm* polystyrene particles were evaporated on SU-8 photoresist. Particles were seeded at concentrations of 0.02% and 0.2% by volume. Deposited droplet volumes were 1 μL. Droplets were exposed to external DC electric fields of either +160 *V* or -160 *V* for a total of six experimental cases. Tungsten ground wires 22 μm in diameter were used to ground the droplets

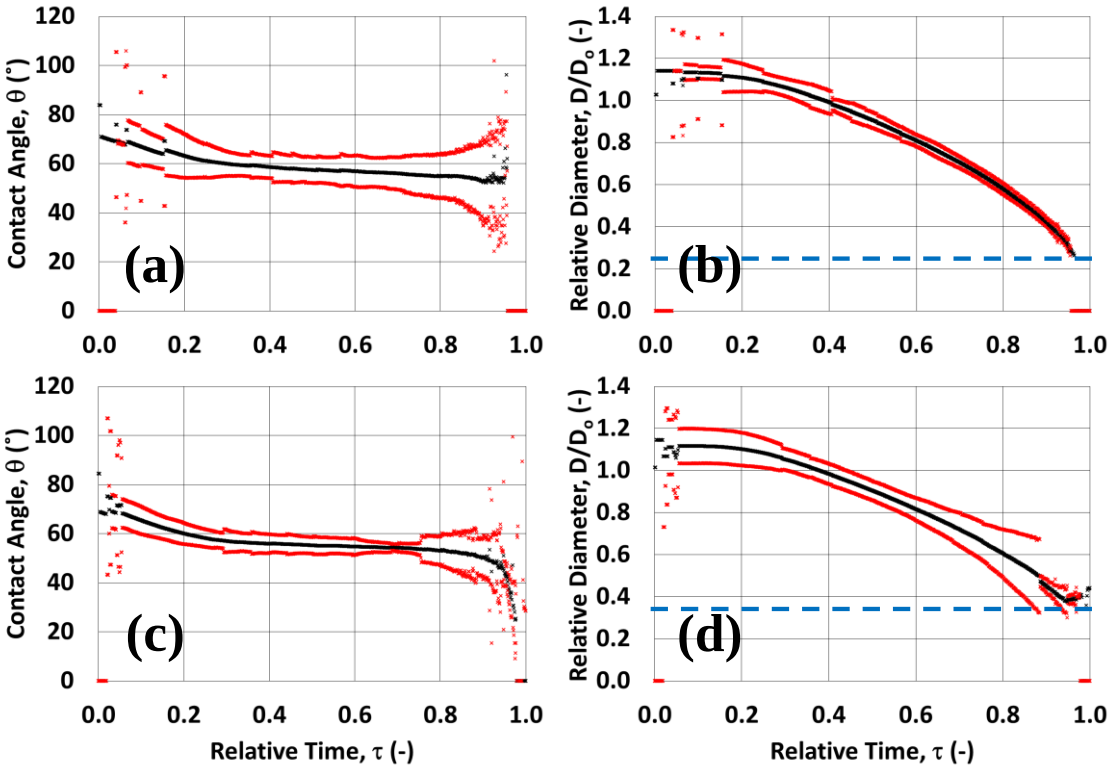

Figure 4.9 Transient droplet profiles during the evaporation under actuation at +160 *V* DC of DI water droplets seeded with 25 *nm* polystyrene particles at concentrations of (a,b) 0.02% and (c,d) 0.2% by volume. Mean values are shown in black, and three standard deviations above and below are shown in red.

during evaporation. A minimum of five trials were performed for each case. Results were compared across cases and to the DI water droplet results to observe the impact of particle presence and concentration on actuated transient evaporative behavior.

The contact angles and diameters of the evaporating 0.02% and 0.2% polystyrene-laden droplets are summarized in Figures 4.9 and 4.10 which present the positively and negatively actuated data, respectively. Both concentrations at both polarities exhibit similar transient behavior as compared to the actuated DI water droplets (Fig. 4.8) through the first 80% of evaporation. Further, the positive and negative cases exhibit the same unexpected difference in behavior of receding smoothly or in a slip-stick pattern through the majority evaporation.

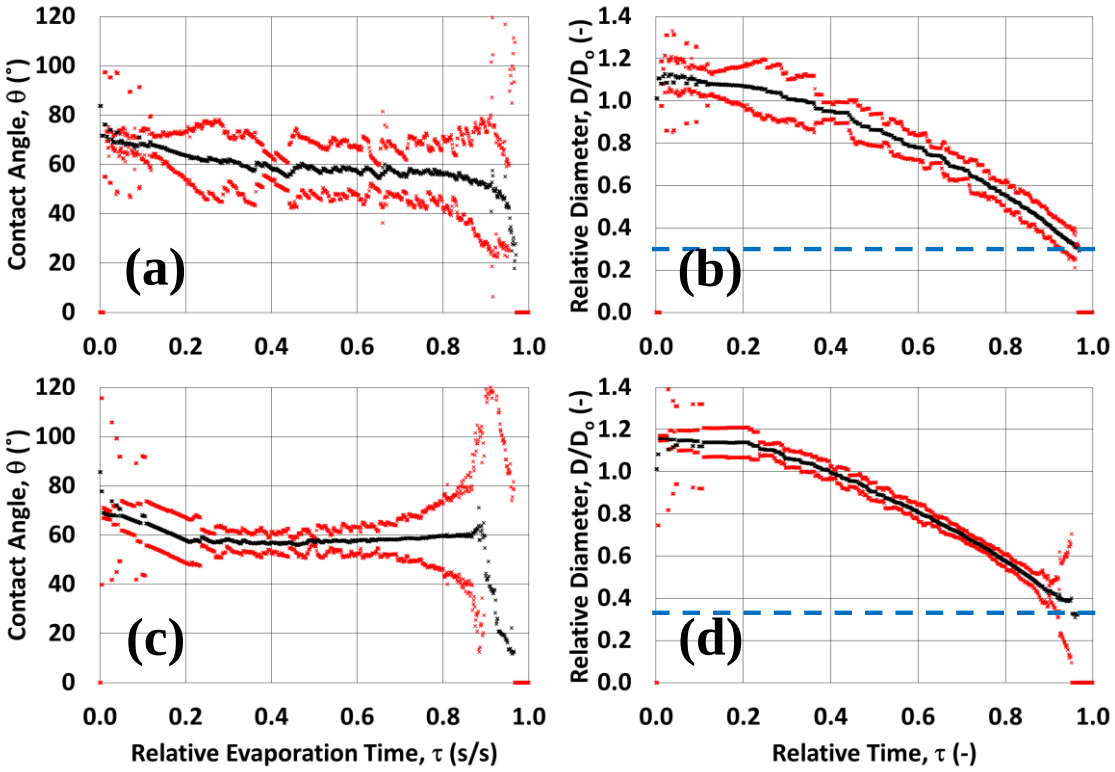

Figure 4.10 Transient droplet profiles during the evaporation under actuation at -160 *V* DC of DI water droplets seeded with 25 *nm* polystyrene particles at concentrations of (a,b) 0.02% and (c,d) 0.2% by volume. Mean values are shown in black, and three standard deviations above and below are shown in red.

In the positively actuated droplets, droplets of both concentrations continue receding in a CCA regime until 95% through evaporation after the initial CCD regime. At this point, the 0.02% droplets cannot be measured due to limitations of the goniometry system [33]. The 0.2% droplets are observed to complete their evaporation in a mixed regime. The negatively actuated polystyrene-laden droplets likewise differ from the negatively actuated DI water droplets beyond 80% of evaporation. Droplets of both concentrations continue to recede in a slip-stick pattern until approximately 90% of the way through evaporation. Beyond this point, both appear to exhibit mixed evaporation regimes until contact angles recede below the measurement threshold of the goniometer.

Table 4.4: Contact angles and pinning forces of actuated polystyrene-laden DI water droplets.

Droplet Type	Initial Angle	Receding Angle	Pinning Force
+160 *V*, 0.02%	71°	57°	15.8 *mN/m*
+160 *V*, 0.2%	70°	56°	15.6 *mN/m*
-160 *V*, 0.02%	71°	54°	18.9 *mN/m*
-160 *V*, 0.2%	69°	56°	14.5 *mN/m*

It does not appear that particle presence at these concentrations had a significant impact on transient droplet behavior. The pinning forces prior to transitioning out of the initial CCD regime, as calculated by Equation 4.9, are summarized in Table 4.4 for all of the actuated polystyrene-laden droplet cases. Pinning forces are fairly similar across all cases at approximately 16 *mN/m*. The pinning force of each individual case is within 20% of this value.

Representative images of depositions left by the positively and negatively actuated 0.02% and 0.2% polystyrene-laden droplets are shown in Figure 4.11. All depositions appear approximately the same size, 500 μm in diameter, and have distinct coffee-ring formations. Most of the particles are deposited at the periphery, and far less deposition appears toward the center regions. This suggests electrophoretic migration is negligible, but further analysis comparing the electrophoretic and evaporative flows is necessary to quantify this effect [44]. The higher concentration depositions have significantly thicker bands of deposition, 30 μm, at the periphery as compared to the lower concentration ones, 10 μm. This is to be expected if the droplets are seeded with more particles and the final depositions are the same size.

Actuation polarity does not appear to influence the final deposition pattern in the higher concentration case. Interestingly, both polarities of 0.2% droplets left similar depositions despite exhibiting different behaviors during evaporation. In the lower concentration, the positively actuated droplets tend to leave a trail of deposition spiraling toward the deposition center. This was observed in the majority of the positively actuated 0.02% cases, and it was not observed in any of the negatively actuated ones. One possibility for this difference may be that the actuation

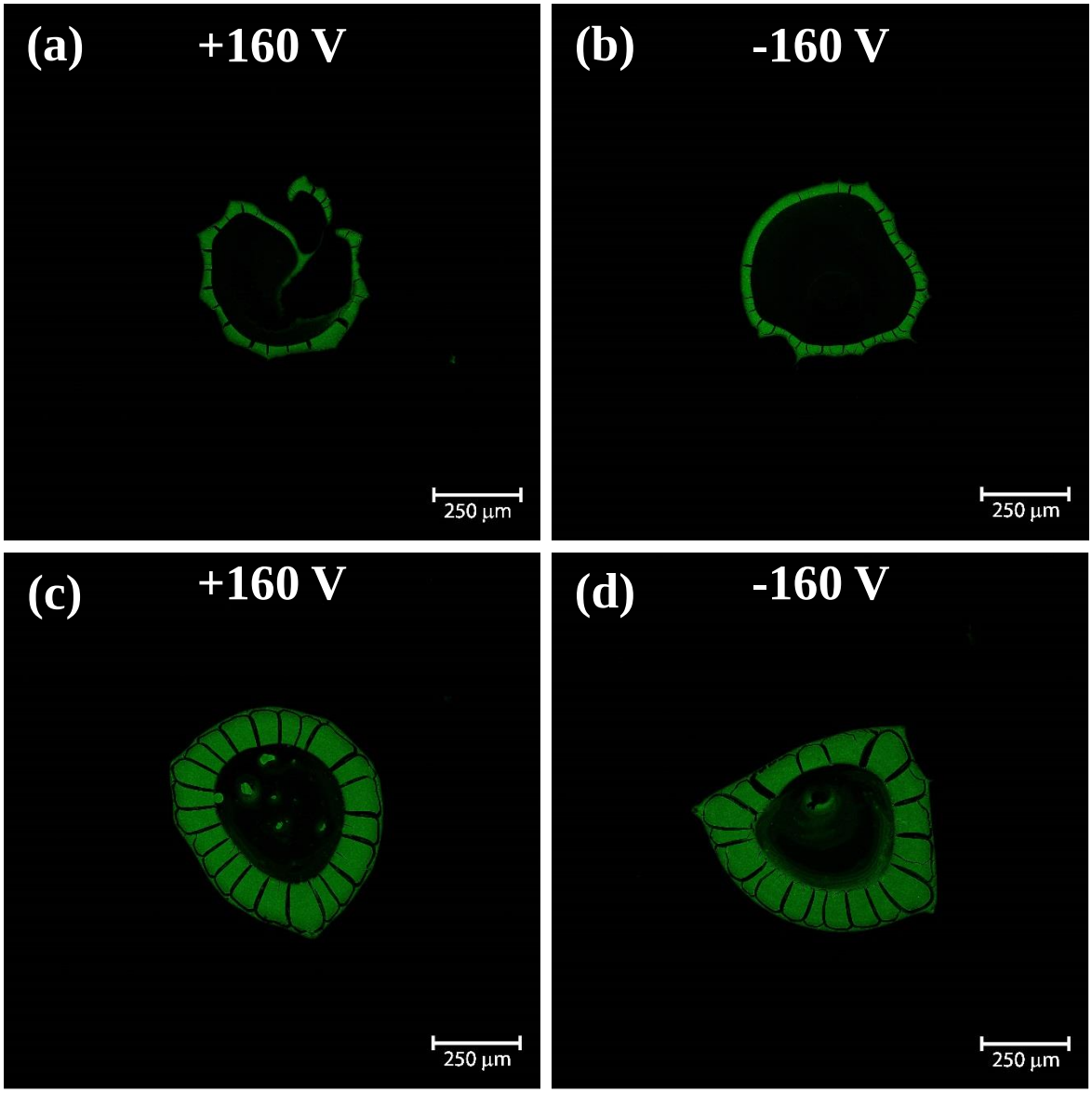

Figure 4.11 Representative depositions patterns left after evaporation of DI water droplet seeded with 25 *nm* polystyrene particles at concentrations of (a,b) 0.02% and (c,d) 0.2% by volume. Droplets were exposed to actuation polarities of (a,c) +160 *V* DC and (b,d) -160 *V* DC during evaporation.

polarity influences how particles interact with the grounding wire at lower particle concentrations. It could also be the result of a weak electrophoretic effect. Further study is necessary to understand this trailing phenomenon more completely. A comparison of the evaporative and electrophoretic flows similar to that done in [44] is necessary to quantify the impact of electrophoresis.

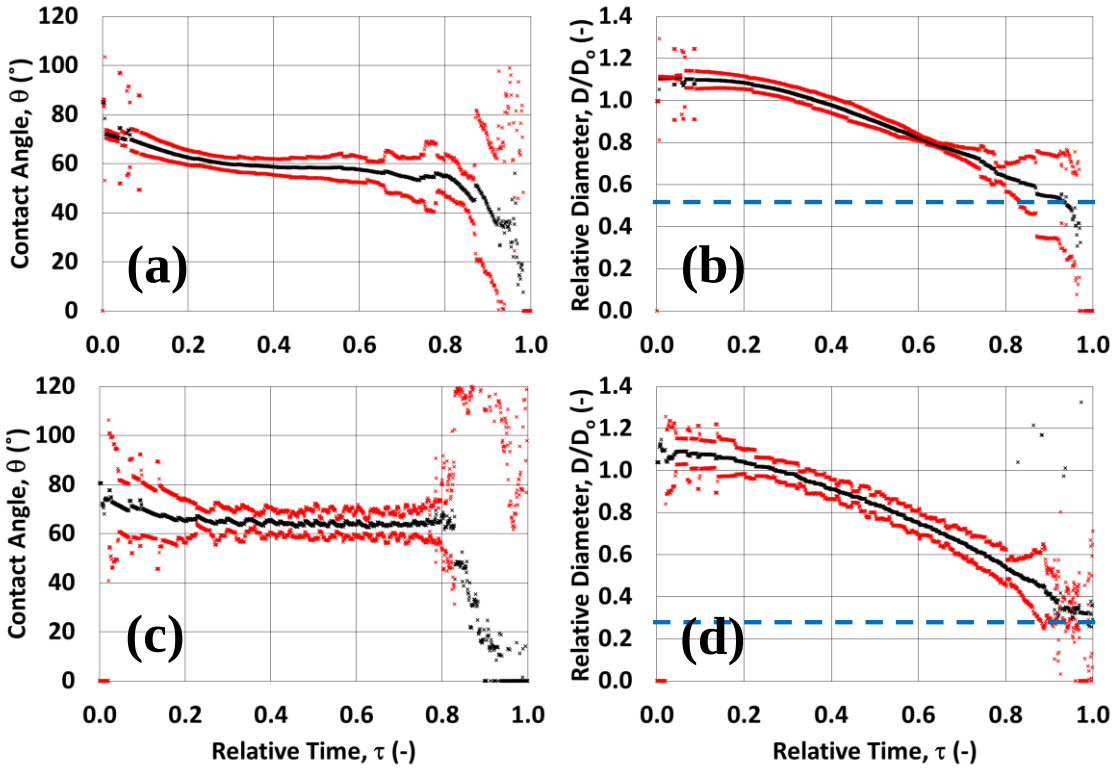

Figure 4.12 Transient droplet profiles during the evaporation under actuation at +160 *V* DC of DI water droplets seeded with 25 *nm* polystyrene particles at a concentration of 0.05% by volume. Trials from (a,b) were performed on the same device as the trials in Figures 4.9 and 4.10. Trials from (c,d) were performed previously on a different device. Mean values are shown in black, and three standard deviations above and below are shown in red.

As part of the study of actuation polarity, droplets were also seeded at 0.05% by volume and evaporated under both positive and negative actuation. Two sets of trials, one positive and one negative, similar to those described for the 0.02% and 0.2% concentrations were performed on the same device. The same two cases were also performed on a different device using a similar setup earlier in the investigation. The only exception was that the cases on the earlier device utilized an 80 μm nichrome ground wire.

The transient data from each of the four data sets is shown in Figures 4.12 and 4.13. The droplets on the newer device used in the majority of the polarity study appears relatively similar to the 0.02% and 0.2% positively and negatively actuated droplets. However, there is a distinct

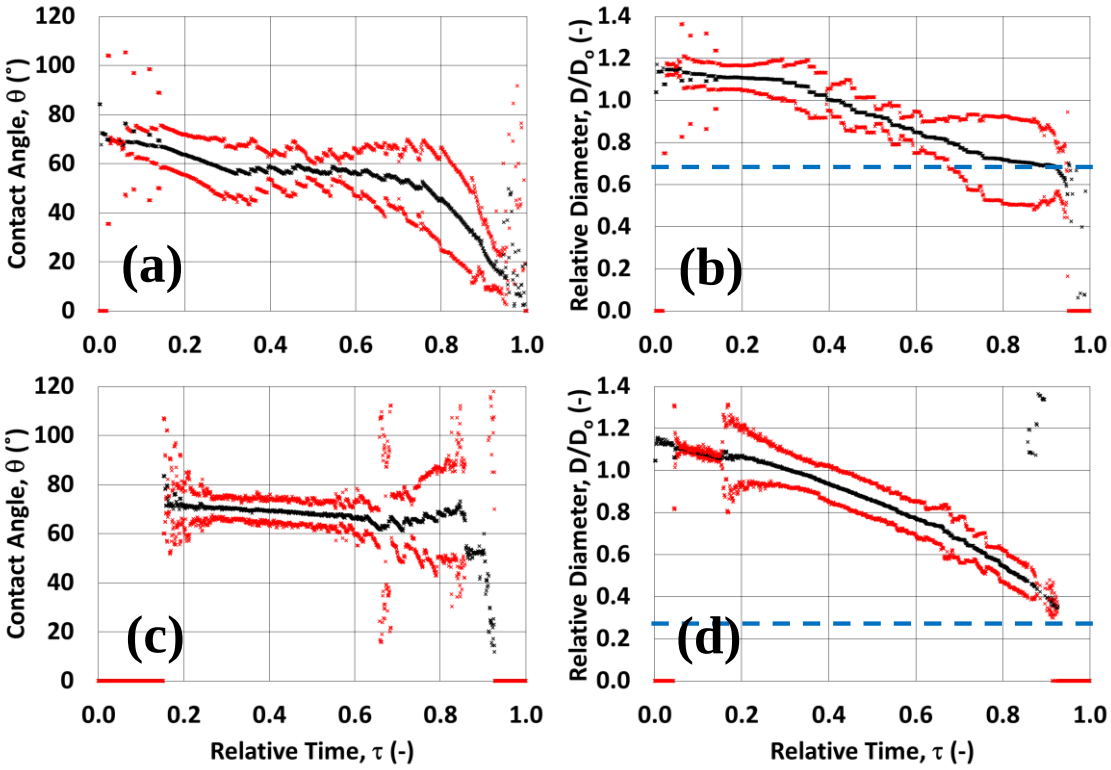

Figure 4.13 Transient droplet profiles during the evaporation under actuation at -160 *V* DC of DI water droplets seeded with 25 *nm* polystyrene particles at a concentration of 0.05% by volume. Trials from (a,b) were performed on the same device as the trials in Figures 4.9 and 4.10. Trials from (c,d) were performed previously on a different device. Mean values are shown in black, and three standard deviations above and below are shown in red.

difference in the transient behavior when comparing the results from the newer device to those on the older device. In the positive cases, droplets on the newer device appear mobile on the surface through the majority of evaporation, while those on the older device primarily exhibit slip-stick behavior. This flips in the negative cases. Here, droplets on the newer device slip-stick through most of evaporation while those on the older device appear more mobile through evaporation.

Representative images from each of the four data sets of 0.05% droplets are shown in Figure 4.14. Again, there is a very distinct difference in deposition pattern when comparing the results on the two devices. Depositions on the older devices appear approximately the same whether actuated with a positive or negative voltage similar to the deposition patterns observed in

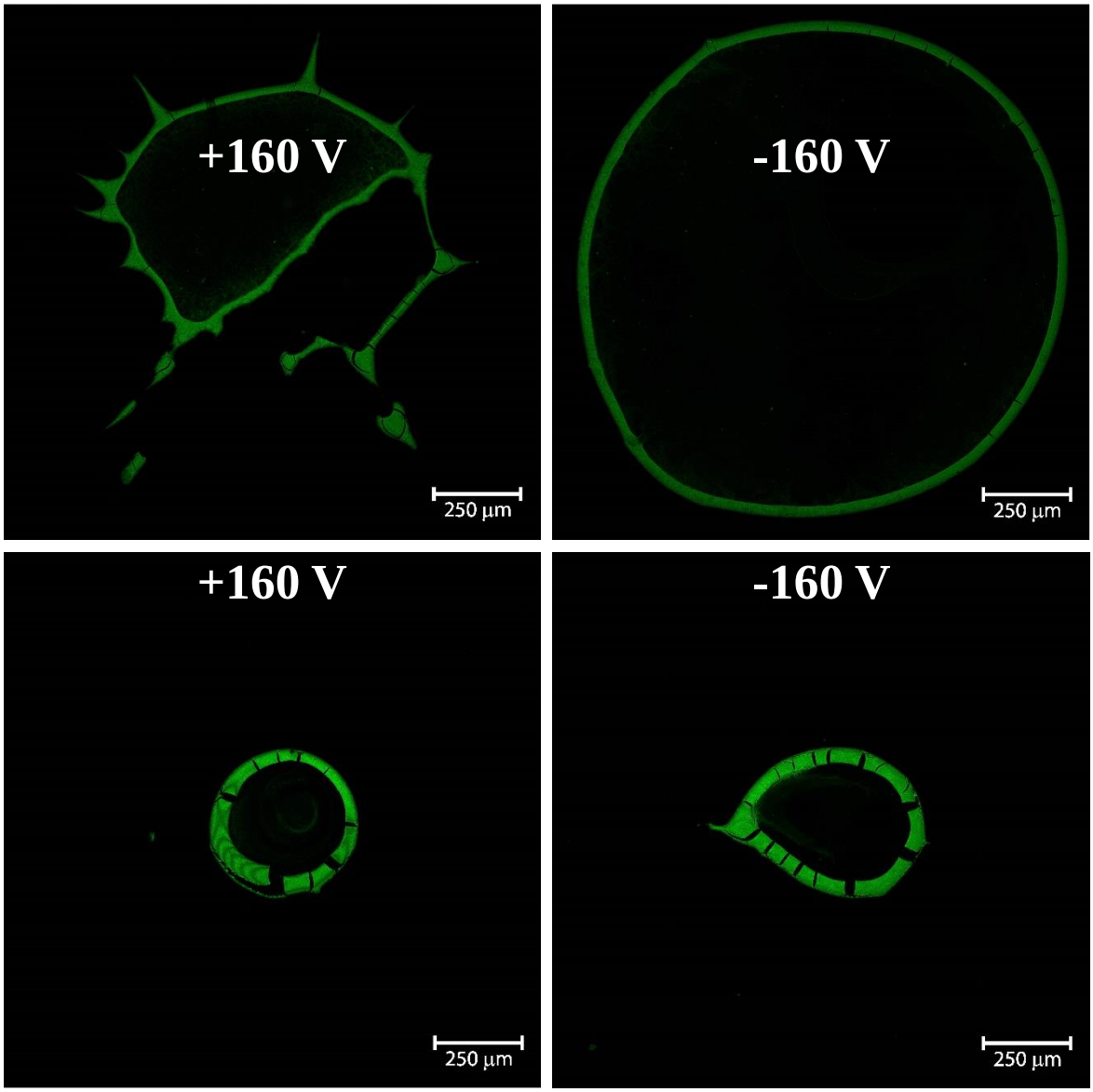

Figure 4.14 Representative depositions patterns left after evaporation of DI water droplet seeded with 25 *nm* polystyrene particles at concentrations of 0.05% by volume (a,b) on an older device and (c,d) on the newer device also used for the 0.02% and 0.2% trials depicted in Figure 4.11. Droplets were exposed to actuation polarities of (a,c) +160 *V* DC and (b,d) -160 V DC during evaporation.

the 0.02% and 0.2% droplets on the newer device (Fig. 4.11). Further, they appear to transition between the 0.02% depositions and the 0.2% depositions. They are of similar size, and the band thickness appears to be somewhere between that of the other two concentrations. The depositions

on the newer device, however, are very different. Both polarities leave depositions roughly twice the diameter of the other concentrations. The negatively actuated droplets leave distinct coffee rings with very little deposition inside or outside of the ring. The positively actuated droplets still form a ring. However, they also leave a number of distinct deposition tendrils that extend radially outward from the coffee ring. This may be evidence of surface inhomogeneities on the device that promoted local pinning. Additionally, they exhibit an inward trail of deposition somewhat similar to those observed in the positively actuated 0.02% droplets.

The significant differences in transient behavior and final deposition patterns observed in the 0.05% droplets on the two different devices is of some concern. However, it is not an uncommon problem in microfluidics. Repeatability is often cited as an issue inhibiting microfluidic technology adoption [57,58]. An examination of the device fabrication process and additional testing on more devices are necessary to confirm device and droplet behavior consistency, respectively.

5.0 CONCLUSIONS

5.1 Summary

This investigation seeks to demonstrate the importance of particle selection on the coffee-ring effect for multiple particle types and sizes. To this end, droplets seeded with several sizes of polystyrene particles as well as titanium oxide were evaporated on SU-8 photoresist substrates. Droplet interfaces were recorded during evaporation to observe the contact line behavior exhibited and to provide insight into the evaporation dynamics occurring within the droplet. Final deposition patterns left after the completion of evaporation were also imaged in order to observe the particle distributions produced. A custom MATLAB script was used in order to analyze the depositions and quantify the radial distribution profiles to compare depositions between different cases. Particle selection was found to affect the pinning behavior and receding contact angles exhibited during evaporation and the intensity distribution, uniformity, and repeatability of the resulting particle depositions after evaporation.

Experimental results suggest that the size of carboxylate-modified polystyrene particles plays an important role in colloidal deposition in evaporating droplets. Unseeded deionized (DI) water droplets and ones seeded with 25 *nm*, 63 *nm*, and 1.1 μm polystyrene particles at a volumetric concentration of 0.05% were deposited and evaporated on SU-8 photoresist. Interestingly, the presence and size of these particles had little impact on the contact line dynamics of the droplet for the first 90% of the evaporation time. However, in the final 10% of evaporation, smaller particle sizes were observed to exhibit late-stage pinning. As a result, particle size did not have a significant effect on the size of the final deposition, but it did affect particle distribution.

Smaller polystyrene particles formed distinct coffee-ring formations. This appears to be

the result of late-stage pinning during evaporation [53,54]. Particles concentrate at the periphery over time and eventually form a ring that can impede further motion of the contact line. Deposition patterns left by 1.1 μm particles were found to be more uniform. Repinning of the contact line in these cases was not observed, so the outward evaporative flow that drives ring formation was never reactivated.

Gravitational effects may also play a role in the uniformity of the deposition pattern in these cases. A ratio of the evaporation time to the characteristic settling time, Sr_z, was computed for each case. Particle settling appears to be negligible for the 25 *nm* and 63 *nm* particles which have very small ratios. However, the 1.1 μm particles have a ratio not much less than 1 (0.043). This suggests that settling may have a non-negligible impact on colloidal transport and some of the particles in the droplet may settle to surface before being carried to the contact line. This would delay the concentrating of particles at the periphery that drives late-stage pinning. Due to the fact that the droplet height decreases over time, the calculated characteristic settling time is overestimated and the true ratio may even be slightly larger. Further, not all particles within the droplet must traverse the entire droplet height in order to settle to the substrate surface.

Another possible cause of the differences in deposition distribution is interface capture. The speed of the droplet interface during evaporation was calculated and compared to the approximate diffusion speed of the three sizes of polystyrene particle. The interface speeds were similar for each case, but diffusion speed varied inversely with particle size. The 25 *nm* and 63 *nm* particles can diffuse more quickly than the interface collapses. However, the interface collapses approximately 1.4 times faster than the 1.1 μm particles can diffuse. This would result in a collection of these larger particles across the droplet interface over time and could contribute to deposition uniformity.

Particle type was observed to have a more dramatic impact on droplet profile behavior as evaporation proceeded. DI water droplets seeded with 25 *nm* polystyrene and 21 *nm* titanium oxide particles at a volumetric concentration of 0.02% were deposited and evaporated on SU-8 photoresist. Polystyrene-laden and titanium oxide-laden droplets both exhibited similar initial contact angles and diameters. However, the addition of titanium oxide particles was observed to increase the pinning effect at the droplet periphery and extend the duration of the constant contact diameter (CCD) evaporation regime initially exhibited by both cases. Polystyrene-laden droplets evaporated until reaching a receding contact angle of 75°, while titanium oxide-laden droplets remained until reaching a receding contact angle of 44°. The calculated pinning force prior to the slip out of the initial CCD regime was nearly three times higher for titanium oxide-laden droplets than polystyrene-laden ones. While polystyrene droplets then entered a constant contact angle (CCA) evaporation regime, the titanium oxide-laden droplets exhibited a slip-stick pattern as they receded.

The particle type used also resulted in distinct differences in both size and distribution in the final depositions. While both droplets began evaporating at similar diameters, titanium oxide-laden droplets produced patterns approximately three times larger in diameter than the polystyrene-laden droplets. The polystyrene patterns formed distinct coffee rings. The titanium oxide patterns were more complex with a thinner outer ring of material bounding the deposition area and a thicker partial ring subdividing it into two regions. In the larger region, deposition coated the substrate relatively uniformly. Far less material was deposited in the smaller region, though several additional faint rings of titanium oxide were visible. These results seem to suggest that titanium oxide particles may adhere to the surface more strongly than polystyrene particles. Particle adhesion at the contact line may account for the increase in the pinning force, while

increased deposition toward the center of the pattern suggest that particles adhere to the entire surface instead of being carried to the contact line and primarily depositing there.

For droplets of both particle types, the time for a particle to reach the surface due to gravitational effects is more than two orders of magnitude longer than the evaporation time of the droplet. This would indicate that gravitational effects do not have a significant impact on deposition behavior. Further, both types of particles can diffuse several times faster than their droplet interfaces can collapse. This suggests that neither type of particle collects across the droplet interface during evaporation. Instead, behavioral differences exhibited by the two particles may be contributable to electrical effects. Electrical forces are known to influence particle-particle and particle-surface interactions. Changes in profile evolutions and final depositions between the two particle types could be driven by the different electrical properties of the two different particle materials.

Preliminary experimental evidence gathered here suggests that DC voltage polarity may affect evaporation dynamics. Pure DI water droplets and those seeded with 25 *nm* polystyrene particles at volumetric concentrations of 0.02% and 0.2% were deposited on SU-8 photoresist. Positive and negative DC electric fields were applied to the droplets as they evaporated. Contact angles in all cases were approximately 70° once the voltage was applied. The receding contact angle exhibited in all cases was approximately 55°. These are both lower than the initial and receding contact angles exhibited by unactuated DI water droplets, 89° and 73°, respectively. A reduction in the initial angle is expected due the application of an electrowetting force at the contact line [24]. The receding angle is also expected to decreases with applied voltage [29]. Both positively and negatively actuated droplets initially pin and evaporate in a CCD regime for the first 30% of evaporation. Beyond this point, positively actuated droplet continue in a CCA regime

through the majority of evaporation. Negatively actuated droplets instead slip and stick repeatedly. This suggests that actuation polarity can impact droplet mobility on a substrate. However, a calculation of the pinning forces for each case suggests that polarity does not significantly impact the maximum pinning force exhibited prior to depinning. Interestingly, the polarity differences were observed in the particle-free and particle-laden cases alike. This suggests that the behavior is not the result of an effect of the polystyrene particles. It may be that the electric field is having an unexpected interaction with the tungsten ground wire inserted into the droplets. If this interaction introduces additional particles into the droplet, it could change the internal electrical interactions [36]. Differences in a ground wire reaction at each polarity could possibly contribute to the changes in droplet profile behavior during evaporation.

Actuation polarity was observed to have only a minimal impact on the deposition patterns produced. Droplets of both concentrations and actuation polarities produced depositions of similar sizes with distinct coffee ring formations. Higher concentration droplets produced rings with thicker bands of material. At the lower concentration, positive actuation resulted in an extra inward trail of deposition in more than half of the depositions. This trail was not present in any of the negatively actuated depositions at this concentration or in either of the higher concentration cases. No differences were observed based on actuation polarity in the depositions left by the more concentrated droplets. The trail presence at the lower concentration under positive actuation may again be due to an unknown interaction with the ground wire used. No case exhibited deposition patterns that would result from downward electrophoretic particle migration as was previously observed with titanium oxide-laden droplets [44]. This result is not entirely surprising since electrophoretic forces are a function of particle charge and polystyrene particles were expected to be more weakly charged than titanium oxide ones.

5.2 Contributions

This investigation has further characterized the effects of particle selection on colloidal droplet desiccation. A method for quantifying the deposition distribution patterns after evaporation was developed for comparing particle cases. Deposition areas are identified in captured images and isolated from any included background data. Deposition intensities are measured in a number of annular sectors created from divisioning the droplet area both radially and azimuthally. Radial intensity distributions, averaged around all azimuthal positions, are then calculated. These can quantify the increase of intensity at the periphery of a ring deposition and the uniformity across a spot deposition. Multiple profiles can be analyzed in a single composite profile to quantify the deposition variation from droplet to droplet.

It was experimentally observed that larger polystyrene particles, on the order of a micron in diameter, tended to leave more uniform deposition patterns than nanoscale particles. Larger particles can achieve higher Stokes velocities and correspondingly reach the surface faster for deposition in a spot pattern prior to being swept to the periphery by an evaporative flow to form a ring pattern. In the larger particles used here, the characteristic settling time was smaller than, but within two orders of magnitude of, the evaporation time. This suggests that while evaporative flows within the droplet may direct the suspended particles elsewhere, gravitational forces may still play a non-negligible role in bringing particles toward the surface. In the smaller, nanoscale particles investigated, the settling time is three or more orders of magnitude longer than the evaporation time and likely plays an insignificant role in particle deposition. Larger particles also diffuse more slowly than smaller particles and may get captured by the interface of a droplet as it evaporates. Particles may collect across the interface until the it collapses completely and the trapped particles are deposited on the surface. The micron-size particles used here diffuse slower

than their droplet interfaces collapse. This may contribute to the uniformity of deposition at this particle size. The smaller particles can diffuse fast enough to outpace a collapsing droplet interface and are likely not trapped.

It was also observed that contact line dynamics in actuated evaporating could be influenced by actuation polarity. Negative actuation produced a slip-stick pattern to occur throughout the large majority of the droplet profile evolution. Alternatively, positive actuation allowed for more uniform changes in the droplet profile evolution with droplets remaining more mobile on the surface. This occurred in both particle-free DI water droplets and polystyrene-laden DI water droplets. The cause of this profile behavior dependence on actuation polarity is not yet fully understood.

5.3 Future Work

This work sought to characterize the effects of particle size, particle type, and actuation polarity on colloidal transport. This was primarily done by observing the droplet exteriors during evaporation and the depositions left behind after evaporation. Analyses of the droplet profiles and final depositions were used to gain some insight as to how particles moved as their droplets dried, but this was never observed directly. Visualizing the particles within droplets as they evaporated would be incredibly helpful for characterizing the effects of particle selection and could help to confirm hypotheses about particle motion that were drawn from profile and deposition behavior.

While several particle characteristic and actuation parameters were characterized in this work, the mechanisms producing the behavioral difference observed between cases are not yet fully understood. Gravitational effects and interface capture may be of some significance for the motion of larger, micron-size particles, but they likely play only a very minimal role for smaller, nanoscale particles. Other effects, especially in nanoparticle cases, may be at play driving colloidal

transport. For instance, electrical effects are known to influence particle-particle and particle-surface interactions [36], but they have not been characterized in the droplets compositions investigated here. A next logical step toward further understanding the colloidal transport behaviors observed in this work would be to characterize the electrical properties of each type of droplet used. Differences in transient profile behavior and deposition distribution could then try to be related back to differences in specific electrical properties. In particular, this may shed light onto the observed differences between the titanium oxide-laden and polystyrene-laden droplets since the electrical characteristics of two different materials are likely very different as well. The first key properties to measure are the zetapotentials and pH levels of the particle-fluid solutions from which the droplets are drawn. These have not previously been measured for any case. Additional particle types could also be tested to study different particle types and electrical characteristics. These could be new materials that would be ideal to control in evaporating droplets, such as carbon nanotubes for transparent conductive films [21] or DNA for medical testing [1], or they could be variants of the particles already examined here with slightly different properties, such as sulfate-modified polystyrene.

It is also recommended to examine the effects of ground wire material. In the polarity study, positive and negative actuation were observed to result in different transient droplet behaviors during evaporation, even when evaporating particle-free DI water droplets. The cause of this difference is not yet understood, but it may be that the electric field is having an unexpected interaction with the tungsten ground wire used that changes with polarity. Multiple materials have previously been utilized for the grounding wire in electrowetting experiments, such as platinum [38] and copper [44]. Repeating the actuated trials presented using ground wires of these or other materials may reveal how, if at all, the wire material impacts contact line dynamics and colloidal

transport during actuated evaporation. Platinum would be an ideal material to try first, since it is inert. Wire effects should be investigated prior to any other variables under actuation to ensure observed differences are not the result of the ground wire material. If it is discovered that the ground wire material causes the observed differences and another material is less reactive and does not influence evaporation depending on polarity, the new material should be used as the default in all future experiments.

Finally, it is critical to ensure results are repeatable when trials are performed on different devices in order for the droplet behaviors observed to be leveraged for practical applications in the future. Repeatability issues often inhibit microfluidic technology adoption [57,58]. Cases from the particle size and type studies were performed a single device, but these trials should be repeated on others to ensure variations in the device were not contributing to the observed droplet behaviors. The cases from the polarity study were also conducted on a single device, though the 0.05% concentration case was previously performed on a different device as well. Very different results were observed in the profile evolutions during and depositions left after evaporation in the two 0.05% concentration sets conducted. In this case especially, trials should be repeated on multiple devices to ensure observed behaviors are consistent across them. The device fabrication process should also be closely examined to ensure devices are as identical as possible.

REFERENCES

[1] a. N. Chijioke, DNA microarrays and their applications in medical microbiology, Biotechnol. Mol. Biol. Rev. 9 (2014) 1–11. doi:10.5897/BMBR2013.0216.

[2] M.B. Miller, Y.-W. Tang, Basic concepts of microarrays and potential applications in clinical microbiology., Clin. Microbiol. Rev. 22 (2009) 611–33. doi:10.1128/CMR.00019-09.

[3] D.S. Daly, A.M. White, S.M. Varnum, K.K. Anderson, R.C. Zangar, Evaluating concentration estimation errors in ELISA microarray experiments., BMC Bioinformatics. 6 (2005) 17. doi:10.1186/1471-2105-6-17.

[4] G. McHale, Surface free energy and microarray deposition technology., Analyst. 132 (2007) 192–5. doi:10.1039/b617339j.

[5] N. Denkov, O. Velev, P. Kralchevski, I. Ivanov, H. Yoshimura, K. Nagayama, Mechanism of formation of two-dimensional crystals from latex particles on substrates, Langmuir. 8 (1992) 3183–3190. doi:10.1016/j.polymer.2007.12.025.

[6] a. S. Dimitrov, C.D. Dushkin, H. Yoshimura, K. Nagayama, Observations of Latex Particle Two-Dimensional-Crystal Nucleation in Wetting Films on Mercury, Glass and Mica, Languir. 10 (1994) 432–440. doi:10.1021/la00014a017.

[7] R. Blossey, A. Bosio, Contact line deposits on cDNA microarrays: A “twin-spot” effect, Langmuir. 18 (2002) 2952–2954.

[8] V. Bromberg, S. Ma, T.J. Singler, High-resolution inkjet printing of electrically conducting lines of silver nanoparticles by edge-enhanced twin-line deposition, Appl. Phys. Lett. 102 (2013) 214101. doi:10.1063/1.4807782.

[9] Z.P. Yin, Y. a. Huang, N.B. Bu, X.M. Wang, Y.L. Xiong, Inkjet printing for flexible electronics: Materials, processes and equipments, Chinese Sci. Bull. 55 (2010) 3383–3407. doi:10.1007/s11434-010-3251-y.

[10] A. Friederich, J.R. Binder, W. Bauer, Rheological Control of the Coffee Stain Effect for Inkjet Printing of Ceramics, J. Am. Ceram. Soc. 96 (2013) 2093–2099.

[11] M.L. Sin, J. Gao, J.C. Liao, P.K. Wong, System Integration - A Major Step toward Lab on a Chip., J. Biol. Eng. 5 (2011) 6. doi:10.1186/1754-1611-5-6.

[12] M. (U. S.E.P.A. Nawar, Potential Nano-Enabled Environmental Applications for Radionuclides, 2009.

[13] G.M. Whitesides, The origins and the future of microfluidics., Nature. 442 (2006) 368–73. doi:10.1038/nature05058.

[14] D. Janasek, J. Franzke, A. Manz, Scaling and the design of miniaturized chemical-analysis systems., Nature. 442 (2006) 374–80. doi:10.1038/nature05059.

[15] World Bank, Making services work for poor people. World Bank Development Report 2004, (2004). http://jae.oxfordjournals.org/content/13/suppl_1/i142.short.

[16] D.D. Dalma-Weiszhausz, J. Warrington, E.Y. Tanimoto, C.G. Miyada, The Affymetrix GeneChip Platform: An Overview, Methods Enzymol. 410 (2006) 3–28. doi:10.1016/S0076-6879(06)10001-4.

[17] J.L. Brewster, K.B. Beason, T.T. Eckdahl, I.M. Evans, The microarray revolution: Perspectives from educators, Biochem. Mol. Biol. Educ. 32 (2004) 217–227. doi:10.1002/bmb.2004.494032040362.

[18] R.D. Deegan, O. Bakajin, T.F. Dupont, Capillary flow as the cause of ring stains from dried liquid drops, Lett. to Nat. (1997) 827–830.

[19] R. Deegan, Pattern formation in drying drops, Phys. Rev. E. 61 (2000) 475–485. doi:10.1103/PhysRevE.61.475.

[20] A. Nathan, A. Ahnood, M.T. Cole, S. Lee, Y. Suzuki, P. Hiralal, et al., Flexible electronics: The next ubiquitous platform, Proc. IEEE. 100 (2012) 1486–1517. doi:10.1109/JPROC.2012.2190168.

[21] A. Shimoni, S. Azoubel, S. Magdassi, Inkjet printing of flexible high-performance carbon nanotube transparent conductive films by “coffee ring effect,” Nanoscale. (2014) 1–6. doi:10.1039/c4nr02133a.

[22] R.D. Deegan, O. Bakajin, T.F. Dupont, G. Huber, S.R. Nagel, T. a Witten, Capillary flow as the cause of ring stains from dried liquid drops, Lett. to Nat. 389 (1997) 827–829.

doi:10.1038/39827.

[23] R. Deegan, O. Bakajin, T. Dupont, G. Huber, S. Nagel, T. Witten, Contact line deposits in an evaporating drop, Phys. Rev. E. 62 (2000) 756–765. doi:10.1103/PhysRevE.62.756.

[24] J. Berthier, The Physics of Microdroplets, 2012.

[25] H. Hu, R.G. Larson, Analysis of the microfluid flow in an evaporating sessile droplet, Langmuir. 21 (2005) 3963–3971. doi:10.1021/la047528s.

[26] F. Mugele, J.-C. Baret, Electrowetting: from basics to applications, J. Phys. Condens. Matter. 17 (2005) R705–R774. doi:10.1088/0953-8984/17/28/R01.

[27] M. Sundberg, A. Månsson, S. Tågerud, Contact angle measurements by confocal microscopy for non-destructive microscale surface characterization., J. Colloid Interface Sci. 313 (2007) 454–60. doi:10.1016/j.jcis.2007.04.067.

[28] R.G. Larson, Transport and Deposition Patterns in Drying Sessile Droplets, AIChE J. 60 (2014) 1538–1571. doi:10.1002/aic.14338.

[29] F. Li, F. Mugele, How to make sticky surfaces slippery: Contact angle hysteresis in electrowetting with alternating voltage, Appl. Phys. Lett. 92 (2008) 1–4. doi:10.1063/1.2945803.

[30] S.F. Chini, A. Amirfazli, A method for measuring contact angle of asymmetric and symmetric drops, Colloids Surfaces A Physicochem. Eng. Asp. 388 (2011) 29–37. doi:10.1016/j.colsurfa.2011.08.001.

[31] D. Orejon, K. Sefiane, M.E.R. Shanahan, Stick-slip of evaporating droplets: Substrate hydrophobicity and nanoparticle concentration, Langmuir. 27 (2011) 12834–12843. doi:10.1021/la2026736.

[32] B.J. Zhang, J. Park, K.J. Kim, H. Yoon, Biologically inspired tunable hydrophilic/hydrophobic surfaces: a copper oxide self-assembly multitier approach, Bioinspir. Biomim. 7 (2012) 036011. doi:10.1088/1748-3182/7/3/036011.

[33] V. Ragoonanan, A. Aksan, Heterogeneity in desiccated solutions: implications for biostabilization., Biophys. J. 94 (2008) 2212–2227. doi:10.1529/biophysj.107.110684.

[34] K.L. Maki, S. Kumar, Fast evaporation of spreading droplets of colloidal suspensions, Langmuir. 27 (2011) 11347–11363. doi:10.1021/la202088s.

[35] W.D. Ristenpart, P.G. Kim, C. Domingues, J. Wan, H.A. Stone, Influence of Substrate Conductivity on Circulation Reversal in Evaporating Drops, Phys. Rev. Lett. 99 (2007).

[36] R. Bhardwaj, X. Fang, P. Somasundaran, D. Attinger, Self-assembly of colloidal particles from evaporating droplets: Role of DLVO interactions and proposition of a phase diagram, Langmuir. 26 (2010) 7833–7842. doi:10.1021/la9047227.

[37] D. Mampallil, H.B. Eral, D. van den Ende, F. Mugele, Control of evaporating complex fluids through electrowetting, Soft Matter. 8 (2012) 10614. doi:10.1039/c2sm26103k.

[38] H.B. Eral, D.M. Augustine, M.H.G. Duits, F. Mugele, Suppressing the coffee stain effect: how to control colloidal self-assembly in evaporating drops using electrowetting, Soft Matter. 7 (2011) 4954. doi:10.1039/c1sm05183k.

[39] D. Mampallil, D. Tiwari, D. van den Ende, F. Mugele, Sample preconcentration inside sessile droplets using electrowetting., Biomicrofluidics. 7 (2013) 44102. doi:10.1063/1.4815931.

[40] L. Morales, J. Parlange, M. Wu, F.J. Pe, W. Zhang, W. Sang, et al., Surfactant-Mediated Control of Colloid Pattern Assembly and Attachment Strength in Evaporating Droplets Vero n, (2013).

[41] B.M. Weon, J.H. Je, Fingering inside the coffee ring, Phys. Rev. E. 87 (2013) 013003. doi:10.1103/PhysRevE.87.013003.

[42] H. Hu, R.G. Larson, Marangoni effect reverses coffee-ring depositions, J. Phys. Chem. B. 110 (2006) 7090–7094.

[43] P.J. Yunker, T. Still, M. a Lohr, a G. Yodh, Suppression of the coffee-ring effect by shape-dependent capillary interactions., Nature. 476 (2011) 308–11. doi:10.1038/nature10344.

[44] D. Orejon, K. Sefiane, M.E.R. Shanahan, Evaporation of nanofluid droplets with applied DC potential, J. Colloid Interface Sci. 407 (2013) 29–38. doi:10.1016/j.jcis.2013.05.079.

[45] W.C. Nelson, C.C.J. Kim, Droplet Actuation by Electrowetting-on-Dielectric (EWOD): A

Review, J. Adhes. Sci. Technol. 26 (2012) 1747–1771.

[46] D. Klarman, D. Andelman, M. Urbakh, A model of electrowetting, reversed electrowetting, and contact angle saturation., Langmuir. 27 (2011) 6031–41. doi:10.1021/la2004326.

[47] F. Mugele, Fundamental challenges in electrowetting: from equilibrium shapes to contact angle saturation and drop dynamics, Soft Matter. 5 (2009) 3377. doi:10.1039/b904493k.

[48] J. Berthier, K.A. Brakke, Digital Microfluidics, in: Phys. Microdroplets, 1st ed., Wiley-Scrivener, 2012: pp. 293–339.

[49] P.D. Dunning, Controlling the Transient Interface Shape and Deposition Profile Left by Desiccation of Colloidal Droplets on Multiple Polymer Surfaces, 2015.

[50] R. Bhardwaj, X. Fang, D. Attinger, Pattern formation during the evaporation of a colloidal nanoliter drop: A numerical and experimental study, New J. Phys. 11 (2009). doi:10.1088/1367-2630/11/7/075020.

[51] K. Uno, K. Hayashi, T. Hayashi, K. Ito, H. Kitano, Particle adsorption in evaporating droplets of polymer latex dispersions on hydrophilic and hydrophobic surfaces, Colloid Polym. Sci. 276 (1998) 810–815. doi:10.1007/s003960050314.

[52] K. Sefiane, Patterns from drying drops, Adv. Colloid Interface Sci. 206 (2014) 372–381.

[53] T.A.H. Nguyen, M.A. Hampton, A. V. Nguyen, Evaporation of nanoparticle droplets on smooth hydrophobic surfaces: The inner coffee ring deposits, J. Phys. Chem. C. 117 (2013) 4707–4716. doi:10.1021/jp3126939.

[54] B.M. Weon, J.H. Je, Self-Pinning by Colloids Confined at a Contact Line, Phys. Rev. E. 110 (2013).

[55] Y. Li, Q. Yang, M. Li, Y. Song, Rate-dependent interface capture beyond the coffee-ring effect, Sci. Rep. 6 (2016) 24628. doi:10.1038/srep24628.

[56] D.R. Adams, M. Toner, R. Langer, Microflow and crack formation patterns in drying sessile droplets of liposomes suspended in trehalose solutions., Langmuir. 24 (2008) 7688–97. doi:10.1021/la703835w.

[57] C.D. Chin, V. Linder, S.K. Sia, Commercialization of microfluidic point-of-care diagnostic devices, Lab Chip. (2012) 2118–2134. doi:10.1039/c2lc21204h.

[58] L.R. Volpatti, A.K. Yetisen, Commercialization of microfluidic devices, Trends Biotechnol. 32 (2014) 347–350. doi:10.1016/j.tibtech.2014.04.010.

APPENDIX A

Portions of this research have been shared through a number of conference proceedings and presentations as detailed here. Results and discussion on the effects of particle selection presented in Sections 4.1 and 4.2 are currently being prepared for submission to scholarly journals for publication.

A.1 Publications

1. Burkhart, C.T., Maki, K.L., Schertzer, M.J. (2016); Effect of Particle Selection on Nanoparticle Assembly; *International Mechanical Engineering Congress & Exposition 2016, Phoenix, AZ.*
2. Burkhart, C.T., Maki, K.L., Schertzer, M.J. (2016); Observation of Contact Line Dynamics in Evaporating Droplets Under the Influence of Electric Fields; *14th International Conference on Nanochannels, Minichannels, and Microchannels, Washington, DC*.
3. Dunning, P.D., Burkhart, C.T., Schertzer, M.J. (2015); Transient Interface Shape and Deposition Profile Left by Desiccation of Colloidal Droplets on Multiple Surfaces; *International Mechanical Engineering Congress & Exposition 2015, Houston, TX*.
4. Burkhart, C.T., Dunning, P.D., Schertzer, M.J. (2015); Electrowetting on Dielectric (EWOD) Assisted Droplet Desiccation; *13th International Conference on Nanochannels, Minichannels, and Microchannels, San Francisco, CA*.

A.2 Presentations

1. Burkhart, C.T., Schertzer, M.J. (2016); Particle Deposition Manipulation via DC Electric Fields; *8th Annual RIT Graduate Research and Creativity Symposium*.

2. Burkhart, C.T., Dunning, P.D., Schertzer, M.J. (2015); Electrowetting on Dielectric (EWOD) Assisted Droplet Desiccation; *13th International Conference on Nanochannels, Minichannels, and Microchannels, San Francisco, CA*.
3. Burkhart, C.T., Schertzer, M.J. (2015); Electrowetting on Dielectric Assisted Droplet Desiccation; *7th Annual RIT Graduate Research and Creativity Symposium*.

APPENDIX B

B.1 Cleanroom Processing

Section 3.2 outlines the process for creating experimental devices. The following tables (Tables B.1-7) detail the methods and recipes used throughout the processing performed. All work is done in the (SMFL).

Table B.1: SU-8 spin recipe.

Phase	RPM	Ramp (*s*)	Time (*s*)
A	500	10	7
B	3000	10	30

Table B.2: Soft bake recipe.

Phase	Temperature (°*C*)	Time (*min*)
A	95	2.5

Table B.3: Exposure recipe.

Phase	Notes
A	200 mJ/cm^2 dose

Table B.4: Post-exposure bake recipe.

Phase	Temperature (°*C*)	Time (*min*)
A	65	60
B	95	120

Table B.5: Development recipe.

Phase	Notes
A	Immerse in developer for 3 minutes for bulk development
B	Spray with developer for 10 seconds to remove stray undeveloped SU-8
C	Spray with isopropyl alcohol for 10 seconds to remove SU-8 developer
D	Air dry with nitrogen spray gun

Table B.6: Hard bake recipe.

Phase	Temperature (°*C*)	Time (*min*)
A	150	3

Table B.7: Aluminum deposition recipe.

Phase	Notes
A	Pump down device-loaded chamber to a pressure of 5 *mTorr*
B	Presputter for 5 minutes to ready tool for deposition
C	Sputter for 30 minutes to deposit aluminum

APPENDIX C

C.1 Supplemental MATLAB Code

Section 3.4 outlines how a custom MATLAB script analyzes the intensity distributions, and by proxy the particle distributions, in depositions left by a particle-laden droplets. Two different versions of the script were used and are detailed here. The original script was only capable of analyzing closed, circular depositions. As experimentation continued, more exotic deposition patterns were routinely observed. The script was later modified to handle irregularly shaped, as well as circularly shaped, depositions that do not necessarily close.

In order to process the grayscale titanium oxide images, an alternate version of the script was developed to accommodate for the lower contrast images. This script works very similarly to the version for the fluorescent polystyrene depositions. The only difference is that the code shown in Section C.3 replaces the code marked "polystyrene-specific code" toward the beginning of the full script in Section C.2. While the polystyrene code is fairly dynamic, the titanium oxide version is specific to the typical depositions observed in this work. It is tuned to the background intensity, circularity, and relative deposition size each trial tended to exhibit. Changes will likely be needed to utilize it for deposition with alternate characteristics.

Both versions of the script cycle through all of the images in the specified folder and analyze each one. Once the image is read in, and the script runs and described in Section 3.4, it saves two figures and a data file for each image. One figure is the grayscale version of the read image with the identified droplet area and centroid marked. The second figure is the intensity distribution within the deposition. The mean value for each radial position is calculated across all azimuthal positions and plotted along with three standard deviations above and below. The data

file contains the mean deposition intensity and the normalized intensities at each radial position within the deposition. Once all images in a folder are analyzed, a master fie is generated containing all of the normalized intensity data for simplified import into another program for further analysis and plotting.

The polystyrene version has an estimated running time of 24 minutes per image based on 20 radial and azimuthal divisions, 400 contouring iterations, and 12-bit input images with resolutions of 4096x4096 pixels. After altering the code to the titanium oxide version, the code has an estimated running time of four minutes per image based on similar parameters and 8-bit input images with resolutions of approximately 2000x1600 pixels.

C.2 Polystyrene Analysis MATLAB Script

```
close all; clear all; tic
thetadiv=20; % number of azimuthal divisions
raddiv=20; % number of radial divisions
contourit=400; % number of iterations for convex mask contour
myFolder = 'C:\Users\...'; % EDIT THIS LINE WITH IMAGE DIRECTORY

% cycle through all jpg images in the selected folder
filePattern=fullfile(myFolder, '*.jpg');
jpgFiles=dir(filePattern);
for fileloop=1:length(jpgFiles)
    baseFileName =jpgFiles(fileloop).name;
    fullFileName=fullfile(myFolder, baseFileName);
    FileName=baseFileName(1:end-4);

    % ----------------------polystyrene-specific code-----------------------
    % convert to grayscale and generate black and white
    RGB=imread(fullFileName);
    I=rgb2gray(RGB);
    thresh=graythresh(I); % Otsu greyscale threshold

    % generate deposition mask
    BWinit = im2bw(I,thresh); % creates BW image using grayscale threshold
    BWfilt=bwareaopen(BWinit,150); % removes areas smaller than 150 pixels
    BWconvex=bwconvhull(BWfilt,'Union'); % fits a convex polygon
    BW=activecontour(I,BWconvex,contourit,'edge'); % contour convex polygon
    % --------------------------------------------------------------------

    % calculate image properties, show and save mask
    [B,L]=bwboundaries(BW,'noholes');
    boundary=B{1}; % there should only be one region
```

```
figure (1)
imshow(I); hold on;
plot(boundary(:,2),boundary(:,1),'r','LineWidth',2)
STATS=regionprops(BW,I,'MeanIntensity','Centroid','Area','Perimeter');
center=cat(1,STATS.Centroid);
intensity_mean=[cat(1,STATS(1).MeanIntensity)];
plot(center(:,1),center(:,2),'rx','LineWidth',2)
saveas(gcf, [FileName '_1.fig'])
close (figure (1))

% create azimuthal masks and calculate local mean radii
clearvars masks_azimuth
rx=max(abs(boundary(:,1)-center(1,1))); % max deviation in x from center
ry=max(abs(boundary(:,2)-center(1,2))); % max deviation in y from center
Rho=1.1*sqrt(rx^2+ry^2); % maximum radius from center, extra 10 percent
Theta=2*pi/thetadiv; % angular increment
for i=1:thetadiv
    rho2=linspace(0,Rho)'; % draw out each sector in polar coordinates
    rho1=flipud(rho2);
    rho3=ones(300,1)*Rho;
    theta1=ones(length(rho1),1)*(i)*Theta;
    theta2=ones(length(rho1),1)*(i+thetadiv-1)*Theta;
    theta3=linspace((i)*Theta+2*pi,(i+thetadiv-1)*Theta,300)';
    rho=cat(1,rho1,rho2,rho3);
    theta=cat(1,theta1,theta2,theta3);
    xazi=rho.*cos(theta)+center(1,1); % convert to rectangular
    yazi=-rho.*sin(theta)+center(1,2);
    masks_azimuth(:,:,i)=poly2mask(xazi,yazi,size(I,1),size(I,2));
    STATS=regionprops(bwareaopen(masks_azimuth(:,:,i).*BW,5),'Area');
    aziradii(i)=sqrt(2*cat(1,STATS.Area)/Theta); % sector mean
end

% create radial masks and calculate annular sector intensities
clearvars masks_radial;
[xmask,ymask]=meshgrid(-(center(1,1)-1):(size(I,2)-center(1,1)),...
    -(center(1,2)-1):(size(I,1)-center(1,2)));
for i=1:thetadiv
    j=1;
    maskradii(1)=1*aziradii(i)/raddiv;
    masks_radial(:,:,1)=((xmask.^2+ymask.^2)<=maskradii(1)^2);
    % only saves radial masks for current sector
    mask_azirad=masks_radial(:,:,1).*masks_azimuth(:,:,i);
    STATS=regionprops(mask_azirad,I,'MeanIntensity');
    intensity_azirad(i,j)=[cat(1,STATS(1).MeanIntensity)];
    % each row is intensities at a particular azimuthal position
    % each column is intensities at a particular radial position
    for j=2:raddiv
        maskradii(j)=j*aziradii(i)/raddiv;
        masks_radial(:,:,j)=and(((xmask.^2+ymask.^2)>maskradii(j-...
            1)^2),((xmask.^2+ymask.^2)<=maskradii(j)^2));
        mask_azirad=masks_radial(:,:,j).*masks_azimuth(:,:,i);
        STATS=regionprops(mask_azirad,I,'MeanIntensity');
        intensity_azirad(i,j)=[cat(1,STATS(1).MeanIntensity)];
    end
end
intensity_aziradnorm=intensity_azirad/intensity_mean;
```

```
    % normalize intensities to mean image intensity

    % calculate final values for plotting
    final_rad=linspace(.5*100/raddiv,100-.5*100/raddiv,raddiv)'; % halfway
    final_intensity=mean(intensity_aziradnorm)';
    final_stdev=std(intensity_aziradnorm)';

    % plot azimuthally averaged intensity vs. radial position
    FS=20; MS=12;
    figure(2)
    axes('FontSize',FS-5);
    grid on; hold on;
    xlabel('Radial Position (%)', 'FontSize',FS);
    ylabel('Normalized Mean Intensity (-)', 'FontSize',FS);
    title(FileName);
    plot(final_rad,final_intensity+0*final_stdev,'k-','MarkerSize',MS)
    plot(final_rad,final_intensity+1*final_stdev,'r--','MarkerSize',MS)
    plot(final_rad,final_intensity-1*final_stdev,'r--','MarkerSize',MS)
    plot(final_rad,final_intensity+2*final_stdev,'b--','MarkerSize',MS)
    plot(final_rad,final_intensity-2*final_stdev,'b--','MarkerSize',MS)
    plot(final_rad,final_intensity+3*final_stdev,'g--','MarkerSize',MS)
    plot(final_rad,final_intensity-3*final_stdev,'g--','MarkerSize',MS)
    saveas(gcf, [FileName '_2.fig'])
    close (figure (2))

    % prepare data for export, save individual trial data
    output1=[intensity_mean;final_intensity]; % mean and intensities
    output2(:,fileloop)=final_intensity; % combined intensities of all images
    output3(fileloop,:)=FileName; % combined names of all images ran
    save([FileName '_mean_normintens.txt'], 'output1','-ascii')
end

% save combined data and trial order
save(['All Combined - data.txt'],'output2','-ascii')
outputcell = strcat(output3);
fid=fopen('All Combined - labels.txt','w');
for r=1:size(outputcell,1)
    fprintf(fid,'%s\n',outputcell(r,:));
end
fclose(fid);
toc
```

C.3 Titanium Oxide Analysis MATLAB Snippet

```
   % ----------------------------TiO2 Changes-------------------------------
    % invert, remove background, convert to BW
    Iinit=imread(fullFileName); % TiO2 starts as GS
    Iinv=imcomplement(Iinit);
    thresh=0.8*graythresh(Iinv); % Otsu greyscale threshold
    BWinit=im2bw(Iinv,thresh); % creates black and white image from I
    % BWfilt1=bwareaopen(BWinit,50); % filter depending on deposition
    I=Iinv.*uint8(BWinit); % or BWfilt1

    % fit a circle to the deposition
```

```
r1=floor(.82*min(size(I))/2); r2=floor(.92*min(size(I))/2);
[centers, radiuses]=imfindcircles(BWinit,[r1 r2],'Sensitivity',.996);
[radius, maxindex]=max(radiuses); % assumes largest circle is correct
radius=radius*1.05; % increase circle size to capture entire deposition
center=centers(maxindex,:); % takes corresponding center

% generate deposition mask
[xmask,ymask]=meshgrid(-(centers(1,1)-1):(size(I,2)-centers(1,1)),...
    -(centers(1,2)-1):(size(I,1)-centers(1,2)));
BWcircle=((xmask.^2+ymask.^2)<=radius^2);
BWconvex=bwconvhull(BWinit.*BWcircle);
BW=activecontour(I,BWconvex,contourit,'edge'); % contour convex polygon
BW=bwareaopen(BW,50); % removes areas smaller than 50 pixels
% ------------------------------------------------------------------------
```

APPENDIX D

D.1 Summary of Experimental Conditions

Section 4 details three different studies examining the effects of particle size, particle type, and DC voltage actuation polarity on transient profiles and final depositions of evaporating colloidal droplets. At least five trials where a droplet was evaporated and analyzed were performed for each set of conditions. The experimental conditions for each data set are summarized in the following tables (Table D.1-4). The "Device" column in each table identifies the specific device in the Discrete Microfluidics Laboratory (DMFL) that was used for the set of trials. All devices have an upper surface of SU-8 photoresist. The "Conc." column indicates the volumetric concentration (*mL/mL*) of the particle added to initially pure deionized (DI) water to create the droplet solution used. All droplets were deposited at a volume of 1 μL.

Table D.1: Particle size testing matrix.

Date	Device	Particle	Conc.	Wire	Actuation
2/23/16	S3-R1a	DI	n/a	n/a	n/a
2/24/16	S3-R2a	25 *nm* PS	0.05%	n/a	n/a
3/11/16	S3-R10	63 *nm* PS	0.05%	n/a	n/a
3/14/16	S3-R11	1.1 μm PS	0.05%	n/a	n/a

Table D.2: Particle type testing matrix.

Date	Device	Particle	Conc.	Wire	Actuation
2/23/16	S3-R1a	DI	n/a	n/a	n/a
4/12/16	S3-R12a	21 *nm* TiO_2	0.02%	n/a	n/a
4/12/16	S3-R12b	25 *nm* PS	0.02%	n/a	n/a

Table D.3: DI water actuation polarity testing matrix.

Date	Device	Particle	Conc.	Wire	Actuation
3/1/16	S3-R6	DI	n/a	22 μm W	n/a
4/20/16	S4-R1	DI	n/a	22 μm W	+160 *V*
4/20/16	S4-R2	DI	n/a	22 μm W	-160 *V*

Table D.4: Polystyrene-laden actuation polarity testing matrix.

Date	Device	Particle	Conc.	Wire	Actuation
7/31/15	W2L-C1a	25 *nm* PS	0.05%	80 μm NiCr	+160 *V*
7/31/15	W2L-C1b	25 *nm* PS	0.05%	80 μm NiCr	-160 *V*
8/3/15	W2L-C3a	25 *nm* PS	0.05%	80 μm NiCr	+160 *V*
8/4/15	W2L-C3b	25 *nm* PS	0.05%	80 μm NiCr	-160 *V*
5/16/16	S4-R3	25 *nm* PS	0.05%	22 μm W	+160 *V*
5/16/16	S4-R4	25 *nm* PS	0.05%	22 μm W	-160 *V*
5/17/16	S4-R5	25 *nm* PS	0.02%	22 μm W	+160 *V*
5/17/16	S4-R6	25 *nm* PS	0.02%	22 μm W	-160 *V*
5/18/16	S4-R7	25 *nm* PS	0.2%	22 μm W	+160 *V*
5/18/16	S4-R8	25 *nm* PS	0.2%	22 μm W	-160 *V*